

Review

# A Review on Material Selection Benchmarking in GeTe-Based RF Phase-Change Switches for Each Layer

Sheng Qu <sup>1,2</sup>, Libin Gao <sup>1,2,\*</sup>, Jiamei Wang <sup>1,2</sup>, Hongwei Chen <sup>1,2</sup>  and Jihua Zhang <sup>1,2,\*</sup>

- <sup>1</sup> School of Integrated Circuit Science and Engineering, University of Electronic Science and Technology of China, Chengdu 610054, China; qushengqs@126.com (S.Q.); wangjiameiaaa@163.com (J.W.); hwchen@uestc.edu.cn (H.C.)
- <sup>2</sup> State Key Laboratory of Electronic Thin Films and Integrated Devices, University of Electronic Science and Technology of China, Chengdu 610054, China
- \* Correspondence: biner167@sina.com (L.G.); jhzhzhang@uestc.edu.cn (J.Z.); Tel.: +86-(8628)-83206506 (L.G. & J.Z.)

**Abstract:** The global demand for radio frequency (RF) modules and components has grown exponentially in recent decades. RF switches are the essential unit in RF front-end and reconfigurable systems leading to the rapid development of novel and advanced switch technology. Germanium telluride (GeTe), as one of the Chalcogenide phase-change materials, has been applied as an RF switch due to its low insertion loss, high isolation, fast switching speed, and low power consumption in recent years. In this review, an in-depth exploration of GeTe film characterization is presented, followed by a comparison of the device structure of directly heated and indirectly heated RF phase-change switches (RFPCSs). Focusing on the prototypical structure of indirectly heated RFPCSs as the reference, the intrinsic properties of each material layer and the rationale behind the material selection is analyzed. Furthermore, the design size of each material layer of the device and its subsequent RF performance are summarized. Finally, we cast our gaze toward the promising future prospects of RFPCS technology.

**Keywords:** chalcogenides; RF phase-change switches; GeTe; RF performance; thin films



**Citation:** Qu, S.; Gao, L.; Wang, J.; Chen, H.; Zhang, J. A Review on Material Selection Benchmarking in GeTe-Based RF Phase-Change Switches for Each Layer.

*Micromachines* **2024**, *15*, 380.  
<https://doi.org/10.3390/mi15030380>

Academic Editors: José Guadalupe Quiñones-Galván and Laura Patricia Rivera Reséndiz

Received: 21 February 2024  
Revised: 8 March 2024  
Accepted: 9 March 2024  
Published: 13 March 2024



**Copyright:** © 2024 by the authors. Licensee MDPI, Basel, Switzerland. This article is an open access article distributed under the terms and conditions of the Creative Commons Attribution (CC BY) license (<https://creativecommons.org/licenses/by/4.0/>).

## 1. Introduction

In contemporary wireless communication systems such as satellites, radar, mobile communication, and electronic countermeasures, a radio frequency (RF) module serves as an integral front-end component. The rapid evolution of millimeter-wave (MMW) technology has spurred dynamic shifts in wireless network requirements, demanding an increased array of devices for smooth integration into wireless networks. For achieving faster data processing rates, the conventional approach involves assembling various RF front-ends tailored for different devices. However, this method tends to demand more space and incurs higher costs, counter to the development ethos of miniaturization and integration. To accommodate diverse frequencies, communication standards, and functional devices, there arises a heightened requirement for reconfigurable modules or systems. Within these reconfigurable systems, RF switches assume a pivotal role as core devices. Considering factors such as integration compatibility, process complexity, and device size, the commonly employed types of RF switches typically include mechanical switches, semiconductor switches, and Micro-Electro-Mechanical Systems (MEMSs) [1–11].

Mechanical switches show exceptional RF performance within the DC–10 GHz range. Nonetheless, these switches exhibit remarkably slow switching speeds, typically ranging from 2 to 50 ms [1–3]. Furthermore, they tend to be bulky in size. On the other hand, semiconductor switches are better suited for high-speed switch applications and offer ease of integration into semiconductor substrates like silicon and gallium arsenide (GaAs). Although semiconductor switches like Positive–Intrinsic–Negative (PIN) diodes [4–6] and

Field Effect Transistor (FET) switches [7,8] are known for their compact size and cost-effective integration into other front-end RF modules, they are also susceptible to distortion, leakage, voltage breakdown, and high non-linearity. Compared with mechanical switches and semiconductor switches, MEMSs have high isolation and good linearity. However, MEMS technology involves a complex process, high power consumption, and often results in lower yields [9–11]. A recent innovation, the GeTe-based phase-change switch (PCS), has emerged and exhibits promising potential as an RF application candidate. PCSs boast a host of advantages, including superior RF performance, high linearity, enhanced integration capabilities, non-volatile characteristics, and rapid switching speeds. These highly competitive properties position PCSs as an ideal choice for miniaturized and intricate RF components, particularly in millimeter-wave applications. In this paper, the focus is primarily on phase-change switches (PCSs) driven by electrical pulses for switching transitions, while another category of PCSs utilizing optical pulses, specifically laser, will not be extensively discussed. Optical-activated PCSs boast a remarkable feature of ultra-fast switching within 200 ps, coupled with a relatively simple structure compared to electrical-activated PCSs [12–17]. However, future integration poses a challenge due to the requirement of a laser source. On the other hand, electrical-activated PCSs, categorized based on heating methods, include direct heating [18–22] and indirect heating [23–28]. These two types of switches will be discussed in more detail in later chapters.

While there exists a burgeoning report on GeTe-based PCSs, the detailed characteristics of the selected material in each layer remain insufficiently explored. This review aims to consolidate recent edges in phase-change RF switches and comprehensively analyze the structural composition of these switching devices concerning materials. The goal is to significantly augment the future RF performance of PCSs by refining design parameters and optimizing material selection. The subsequent content delves into an in-depth analysis of the materials used in each layer of a PCS, followed by an outlook on future prospects for this technology.

## 2. Selection of Phase-Change Material

### 2.1. The Phase Change of Chalcogenides

Phase-change materials (PCMs) exhibit a distinctive characteristic whereby they can undergo reversible transformations between the amorphous and crystalline states following heat treatment with precise electrical pulses, as depicted in Figure 1a [29–31]. The amorphous configuration signifies a disorganized arrangement of atoms, referred to as short-range ordering, whereas the crystalline state reflects an organized atomic arrangement, known as long-range ordering. The disordered amorphous state features a reduced mean free path for electrons, impeded by scattering, consequently resulting in higher electrical resistance relative to the crystalline state.

When subjected to intense and short-duration pulses, the material's temperature rises rapidly above its melting point ( $T_m$ ) and changes into a liquid state. Subsequent rapid quenching prompts the atoms to solidify with a disordered arrangement, thus completing the transition from the crystalline to the amorphous state. In contrast, the transition from amorphous to crystalline necessitates maintaining the temperature of PCM below the melting point and keeping it above the crystallization temperature ( $T_c$ ) for a certain duration, allowing atoms to reassemble into an organized arrangement, as illustrated in Figure 1a [32,33].

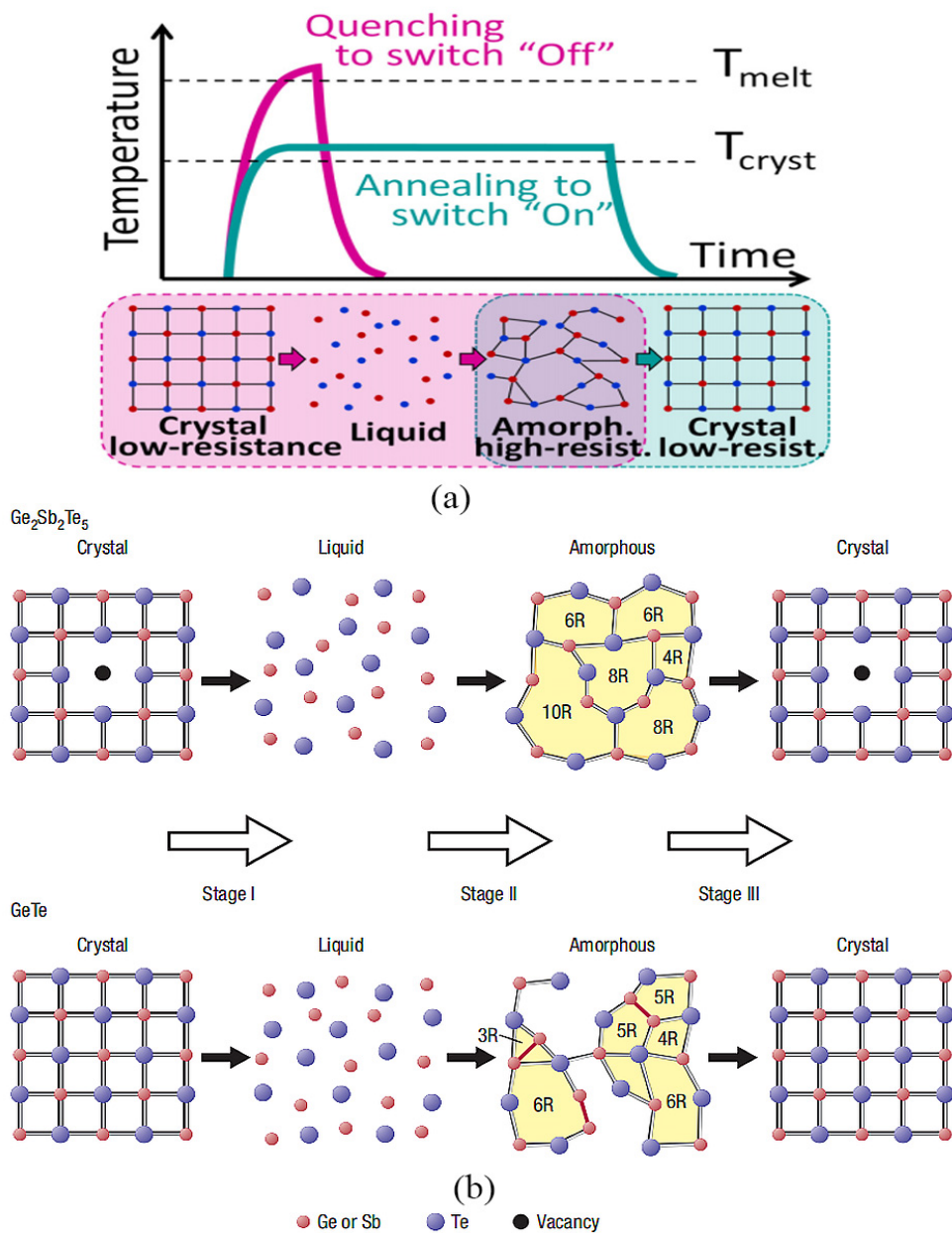


**Figure 1.** (a) Reversible switching of PCM under thermal pulses (adapted from [31]). (b) Schematic presentation of the possible ring structure transformation in the phase changes of crystal–liquid–amorphous and amorphous–crystal in  $\text{Ge}_2\text{Sb}_2\text{Te}_5$  and  $\text{GeTe}$  (adapted from [33]).

Typically, the amorphous state is a highly disordered arrangement of atoms, but the amorphous state of chalcogenide compounds contains some interesting rules of arrangement. Kohara et al. conclude that amorphous  $\text{Ge}_2\text{Sb}_2\text{Te}_5$  is characterized by even-folded ring structures, whereas amorphous  $\text{GeTe}$  has both even- and odd-numbered rings [33]. A diverse array of ring structures exists in  $\text{GeTe}$ , encompassing both even- and odd-numbered formations. As illustrated in Figure 1b, the presence of odd-numbered rings predominantly signifies the existence of homopolar bonds like Ge–Ge bonds, while the prevalence of even-numbered rings indicates a pronounced inclination towards heteropolar bonds, thereby suggesting the absence of Ge–Ge bonds in  $\text{Ge}_2\text{Sb}_2\text{Te}_5$ . The intricate calculations performed further unveil microscopic remnants of the crystal structure within the amorphous state, such as the persistence of even-numbered rings and bond angles approaching 90 degrees. It is noteworthy that although the total pair correlation functions between the amorphous

and crystalline states significantly differ, the amorphous structure retains several distinctive features reminiscent of its crystalline counterpart.

The potential materials mainly used in RF switches are Ge-Sb-Te ( $\text{Ge}_2\text{Sb}_2\text{Te}_5$ ), germanium tellurium (GeTe), antimony telluride (SbTe), and vanadium oxide ( $\text{VO}_2$ ). Currently, a great deal of research work endeavors concerning these materials has predominantly centered around optical storage as well as electrical storage in phase-change memories [34–38], and some of them have already been realized for a wide range of commercial applications, like CD and DVD. In recent years, a growing number of scholars have extended the utilization of these materials towards achieving the functionality of RF switches [12–22,39–44].

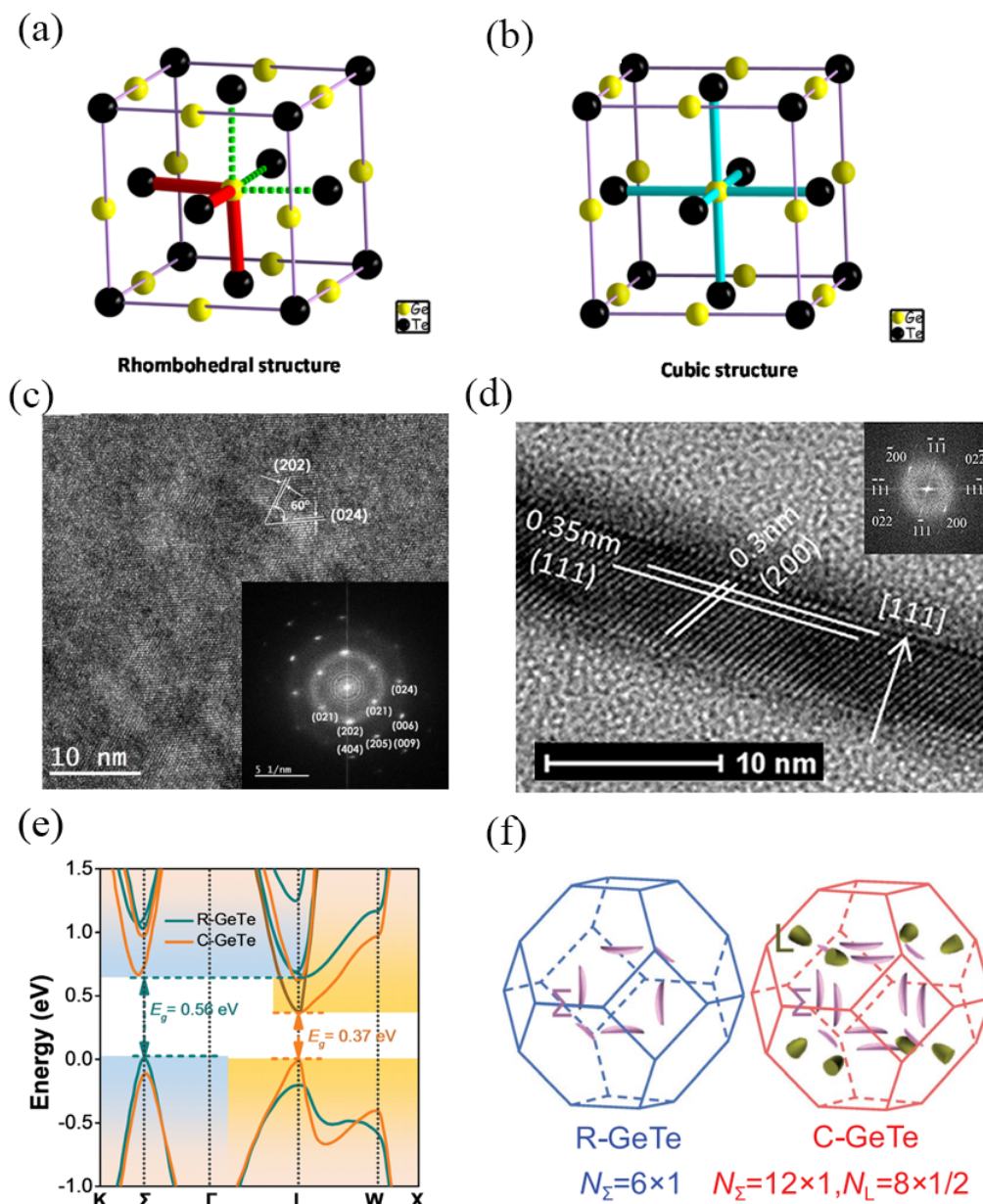
Moon et al. reported the first SbTe phase-change material RF switch with a cutoff frequency ( $F_{\text{co}}$ ) of 4.1 THz [39]. Subsequently, Yalon et al. proposed an indirect heating phase-change RF switch based on  $\text{Sb}_7\text{Te}_3$ , with  $F_{\text{co}}$  of 5 THz, and power and energy density of  $\sim 8 \text{ mW}/\mu\text{m}^2$  and  $\sim 2.4 \text{ nJ}/\mu\text{m}^2$ , respectively [40]. Mennai et al. presented the first  $\text{Ge}_2\text{Sb}_2\text{Te}_5$  phase-change material RF switch with the figure of merit (FOM) of about 450 fs [41]. Pan et al. designed the  $\text{VO}_2$ -based single-pole-single-throw (SPST) switch with the insertion loss  $< 3 \text{ dB}$  at 10 GHz. In addition, the isolation of SPST switch improved to better than 30 dB [42]. Given that GeTe is the most used phase-change material on RF switches, a specific discussion will follow in a later section. Detailed descriptions of the performance about specific switches will be provided in subsequent chapters. Table 1 illustrates the performance outlined in pertinent studies of RF switches. Considering the advantages of phase-change temperature, resistivity, and non-volatility, GeTe thin films dominate RF PCSs, according to the reported literature.

**Table 1.** Relevant properties of  $\text{Ge}_2\text{Sb}_2\text{Te}_5$ , GeTe,  $\text{Sb}_x\text{Te}_y$ , and  $\text{VO}_2$  for PCS.

Phase-Change Material	$\text{Ge}_2\text{Sb}_2\text{Te}_5$	GeTe	$\text{Sb}_x\text{Te}_y$	$\text{VO}_2$
Crystallization temperature $T_c$ ( $^\circ\text{C}$ )	140	190–210	145–150	65–80
Crystalline resistivity ( $\Omega\cdot\text{cm}$ )	$10^{-1}$	$10^{-4}$	$10^{-2}$	$10^{-1}$
$R_{\text{on}}$ ( $\Omega$ )	10	0.9	4.5	10
$R_{\text{off}}$ ( $\Omega$ )	150 k	35.3 k	35 k	10 k
Switching time	270 $\mu\text{s}$	2 $\mu\text{s}$	1.3 $\mu\text{s}$	0.4 $\mu\text{s}$
Non-volatile	Yes	Yes	Yes	No
Ref.	[41]	[16–28]	[39,40]	[42–44]

## 2.2. The Structural Analysis of GeTe

GeTe is categorized as a degenerately doped p-type semiconductor based on its electronic properties. It exhibits two stable states at room temperature, which can be switched repeatedly. As far as the structure of crystalline GeTe is concerned, it was initially hypothesized to correspond to an ideal rock salt structure, commonly referred to as rhombohedral GeTe (R-GeTe). However, it was found that R-GeTe is a distorted face-centered cubic (FCC) as rhombohedral structure, as shown in Figure 2a. GeTe begins to undergo an ordered–disordered transition at a temperature range of 473 K to 673 K [45,46]. When it undergoes homogeneous melting, R-GeTe transitions to cubic GeTe (C-GeTe), which is formed at 693 K and is observed up to 973 K [47]. In the rhombohedral configuration, the Ge atom resides off-center within the octahedron formed by six Te atoms with 3 longer bonds and 3 shorter bonds as red sticks and green sticks as Figure 1a shows, while in the rock salt as well as cubic arrangement, it occupies the central position of the octahedron. In contrast, all Ge-Te bonds exhibit uniform length in the cubic structure, as 6 blue sticks showcased in Figure 2b [48].



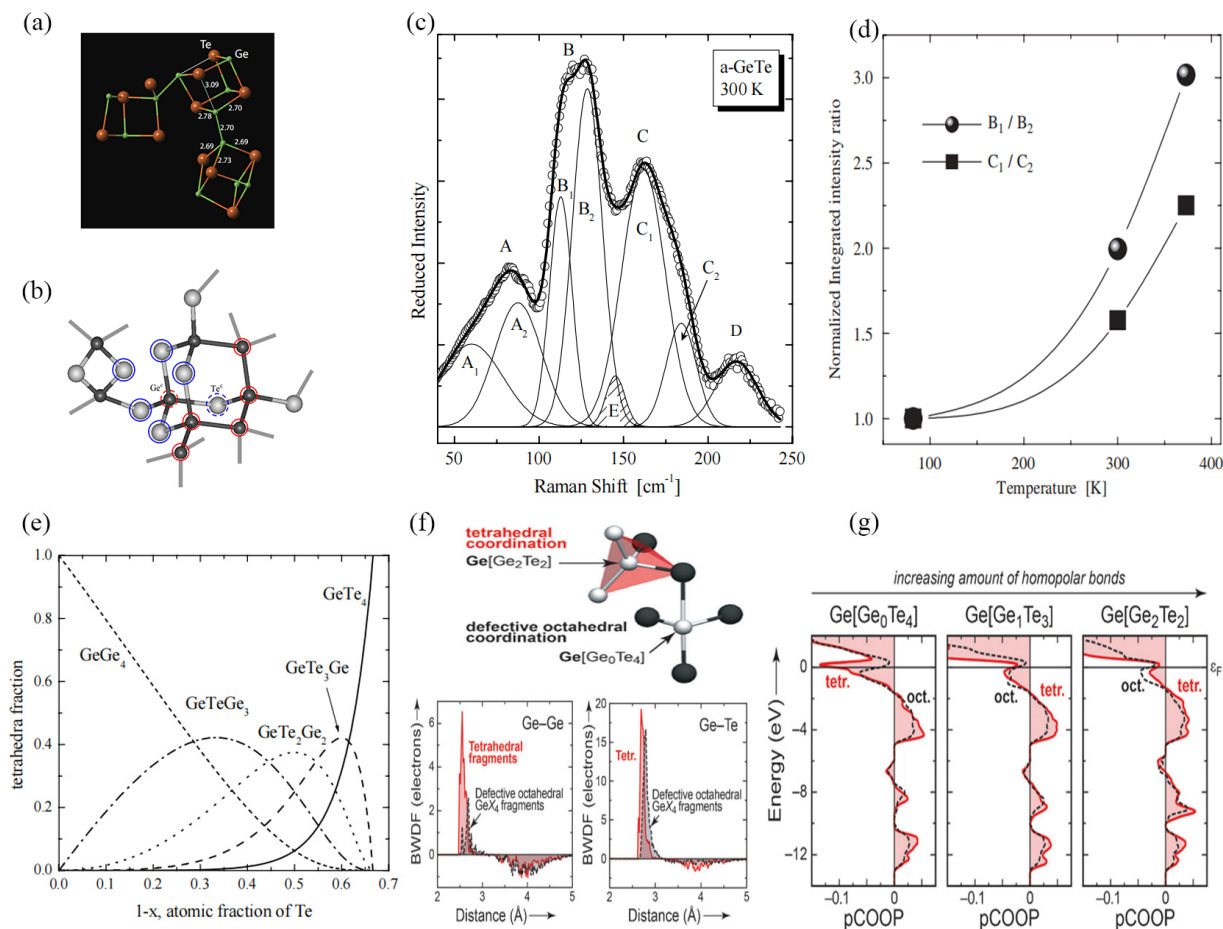
**Figure 2.** Structure of crystalline GeTe: (a) rhombohedral configuration, (b) cubic configuration (adapted from [48]). (c) TEM of GeTe film deposited and annealed at 573 K for 24 h (inset: corresponding FFT) (adapted from [49]). (d) High-resolution TEM images crystalline GeTe film annealed at 673 K (inset: corresponding FFT) (adapted from [50]). (e) Calculated band structures of R-GeTe and C-GeTe, respectively (adapted from [51]). (f) Crystal structure of  $\alpha$ -GeTe in hexagonal setting (note that the space-group symmetry is not hexagonal due to the presence of a threefold, rather than sixfold, rotation axis) (adapted from [52]).

Figure 2c shows the Transmission Electron Microscope (TEM) image of GeTe films deposited at 573 K and annealed for 24 h. The corresponding fast Fourier transform (FFT) patterns (insets in Figure 2c) of the GeTe film indicate a rhombohedral crystal structure (space group R3m). FFT exhibits lattice fingers spaced 3.29, 3.03, 2.10, 1.76, 1.44, 1.88 Å and 1.18 Å from the (021), (202), (024), (006), (404), (205) and (009) planes of the R-GeTe crystal structure (space group R3m), respectively [49]. Figure 2d depicts the high-resolution TEM image of GeTe film annealed in a vacuum furnace at 673 K. In the TEM of crystallite, two sets of planes are observed. Besides the (111) lattice planes with a plane spacing of 3.5 Å, the other exhibits a series of (200) planes with a lattice spacing of 3.0 Å, intersecting with

the (111) planes at an angle of  $55^\circ$ . The corresponding fast Fourier transform (FFT) patterns (insets in Figure 2d) of the GeTe film reveal a face-centered cubic pattern [50], confirming the rock salt structure of the crystallite. Across all crystallites, the (111) planes align parallel to the film surface, suggesting that the preferential orientation of the crystallites within the C-GeTe film lies in the (111) direction along the film thickness. This aligns with previous reports [46].

Figure 2e offers a comparison between the calculated band structures of R-GeTe and C-GeTe. Following the phase transition, the calculated bandgap of GeTe decreases from 0.56 eV (indirect type) in R-GeTe to 0.37 eV (direct type) in C-GeTe [51]. The bandgap in the amorphous state has been reported to be approximately 0.8 eV. This relatively wide bandgap restricts the mobility of charge carriers and thus limits the conductivity of the material. However, upon transitioning to the crystalline state, the bandgap narrows significantly. This narrowing of the bandgap facilitates the movement of charge carriers, leading to a substantial enhancement in the conductivity of the GeTe crystal. Consequently, the narrow bandgap in the crystalline state plays a pivotal role in enabling efficient charge transport within the material, thereby greatly improving its overall conductivity, especially in C-GeTe. The calculated Fermi surfaces in Figure 2f reveal similar crystal structures for R-GeTe and C-GeTe, with nearly identical first Brillouin zones. Additionally, R-GeTe encompasses six full valleys of  $VB\Sigma$ , while C-GeTe comprises twelve full valleys of  $VB\Sigma$  plus eight half valleys of VBL. Consequently, the rhombohedral-to-cubic phase transition significantly augments the band degeneracy in GeTe. Therefore, C-GeTe exhibits superior electronic-transport properties compared to R-GeTe [52,53].

X-ray absorption fine structure (EXAFS) measurements reveal that throughout the amorphization process, the average coordination number of Ge ions decreases from six to four, as demonstrated in studies [54,55]. The motif of amorphous GeTe is rigorously supported by Figure 3a,b [56,57]. Kolobov et al. postulated that Ge resides in a hybrid structure combining aspects of a tetrahedral configuration and a defective octahedral configuration within amorphous GeTe [46]. This structural arrangement undergoes a remarkable transformation throughout the crystallization process, transitioning from a tetrahedral form to a defect-free octahedral form. It is important to note that amorphous GeTe does not exhibit complete disorder. Yannopoulos et al. have studied the temperature-dependent Raman spectra of GeTe [57]. In Figure 3c, the Raman spectra of crystalline GeTe exhibit just two distinctive peaks, aligning with the amorphous B and C peaks (offset by  $\sim 45 \text{ cm}^{-1}$ ). Remarkably, the observed proportional relationship between frequency and energy,  $E(d^{\text{cr}}) < E(d^{\text{a}})$ , aligns with the proposed formula  $E(d^{\text{cr}}) = 0.635E(d^{\text{a}})$ , where  $d^{\text{cr}}$  and  $d^{\text{a}}$  represent crystalline and amorphous bond lengths and  $E$  represents energy [58]. The data depicted in Figure 3d, based on calculations, illustrate an increase in the ratio between the integrated intensity of the  $B_1$  and  $B_2$  bands, as well as the corresponding ratio of the  $C_1$  and  $C_2$  bands when subjecting the material to heat [59]. This observation infers a gradual shift in the composition of the tetrahedral species forming the glassy structure as the amorphous film is heated. This shift leads to the formation of Te-rich tetrahedra at the expense of Ge-rich tetrahedra, thus implying that the atomic arrangement within the primary coordination unit changes as a result of the temperature increase, even below  $T_c$ . A quantitative analysis of the vibration modes was carried out using a Gaussian line fitting method, revealing the presence of five distinct vibration modes. Therefore, the possible tetrahedral combination structure of  $\text{GeTe}_{4-n}\text{Ge}_n$  ( $n = 0, 1, 2, 3, 4$ ) was proposed [57]. This remarkable outcome suggests significant structural re-configurations occurring within the amorphous solid structure, even at temperatures lower than the crystallization temperature. The amorphous structure is delineated by a composition of five tetrahedral combinations: 6.25%  $\text{GeTe}_4$ , 25%  $\text{GeTe}_3\text{Ge}$ , 37.5%  $\text{GeTe}_2\text{Ge}_2$ , 2.25%  $\text{GeTeGe}_3$ , and 6.25%  $\text{GeGe}_4$ . The relative distribution of these five structures is illustrated in Figure 3e.



**Figure 3.** (a) The panel shows Ge and Te atoms that are involved in tetrahedral Ge configurations using DFT simulations (adapted from [56]). (b) Possible mechanism for the amorphous-to-crystal transition (adapted from [57]). (c) Quantitative description of the vibrational modes with the aid of a Gaussian line fit procedure (adapted from [57]). (d) Normalized intensity ratio of the  $B_1$ ,  $B_2$  and  $C_1$ ,  $C_2$  bands as a function of temperature designating the increase of Te-rich tetrahedra with respect to the Ge-rich tetrahedra as temperature is raised (adapted from [59]). (e) Relative distribution of the various types of  $GeTe_nGe_{1-n}$  tetrahedra, as a function of the chalcogenides' atomic fraction. The smaller red dots represent Ge ions and the larger yellow dots represent Te ions (adapted from [59]). (f) Upper part: Structural fragment drawn to emphasize the different coordination motifs found in the amorphous phase. Bottom parts: BWDFs of homopolar (Ge-Ge) and heteropolar (Ge-Te) contacts, according to the coordination environments (adapted from [60]). (g) P-COOP analysis resolved according to  $GeX_4$  motifs in one of the structural snapshots. P-COOPs (per bond) are averaged separately for tetrahedral and defective octahedral motifs (adapted from [60]).

Ab initio molecular dynamics (AIMD) modeling of amorphous GeTe obtained by quenching in the melt revealed a substantial presence of tetrahedrally coordinated germanium atoms. These tetrahedral structures seldom comprise four Te ligands. However, they consistently include at least one homopolar Ge-Ge bond, as sketched in the upper part of Figure 3f [60]. Within tetrahedra, the bond-weighted distribution function (BWDF) of homopolar Ge-Ge contacts (bottom left part of Figure 3f) exhibits a more significant bonding peak at short distances of approximately 2.6, demonstrating that Ge-Ge bonds within tetrahedral formations appear chemically strong, while in octahedral environments, the bottom left part of Figure 3f indicates a lack of significant Ge-Ge bonding as the positive BWDF region is counteracted by an anti-bonding one at longer distances. Regarding heteropolar bonds, the Ge-Te contact nature appears relatively consistent regardless of the local structure, displaying similar BWDF curves in bottom right part of Figure 3f. This

suggests that homopolar bonds bolster tetrahedral configurations in amorphous GeTe but do not notably fortify octahedral arrangements. Left-hand p-COOP (partial Crystal Orbital Population) curves in Figure 3g reveal pronounced instabilities in the tetrahedral GeTe<sub>4</sub> motifs, notably featuring a major anti-bonding peak at the  $\epsilon$ F position. This aligns with the infrequency of pure GeTe<sub>4</sub> tetrahedra observed Figure 3f. Conversely, the presence of one or two homopolar bonds (middle and right-hand panels in Figure 3g) significantly diminishes these antibonding interactions within the tetrahedra. Judging solely from the shape of the p-COOP curves, homopolar contacts seem more conducive to the tetrahedral motif [61].

Recently, it has been argued that the observed “ideal” rock salt structure is the result of the averaging effect, not the result of the local atomic environment. Even at high temperatures, the length of the Ge-Te bond will not be affected [56]. The source of this obvious difference lies in different measurement techniques: X-ray and neutron diffraction produce the overall structure, while EXAFS detects the local surroundings of the atom. As far as the current study is concerned, the precise nature of the phase transition remains a topic of ongoing discussion [62].

### 2.3. Characteristic of GeTe Films

The stoichiometric balance between Ge and Te in GeTe alloy compounds significantly impacts resistivity. GeTe films with diverse composition ratios exhibit considerable variations in crystalline and amorphous resistivity [63]. Typically, the ratio of amorphous resistivity to crystalline resistivity spans three to six orders of magnitude. In the conducted temperature-dependent resistivity experiments on 100 nm thick Ge<sub>x</sub>Te<sub>100-x</sub> films prepared by magnetron sputtering with different GeTe compositions, depicted in Figure 4a,b, it is notable that the Ge<sub>36</sub>Te<sub>64</sub> film displays the most pronounced resistivity shift between its amorphous and crystalline states, alongside minimal programming requirements [64,65]. The Ge<sub>44</sub>Te<sub>56</sub> film demonstrates the lowest resistivity, with crystallization occurring at approximately 190 °C. In Figure 4c,d, X-ray diffraction (XRD) analyses of the five compositions are depicted. For Te-rich samples like Ge<sub>36</sub>Te<sub>64</sub> and Ge<sub>44</sub>Te<sub>56</sub>, as shown in Figure 4c, the crystalline rhombohedral GeTe and hexagonal Te evidence appears at 250 °C. GeTe and Te crystallization happens simultaneously at the same temperature. In proximity to the 50:50 stoichiometric composition, the Ge<sub>53</sub>Te<sub>47</sub> sample displays only characteristic rhombohedral GeTe peaks. Conversely, for Ge-rich samples, as shown in Figure 4d, the segregation of cubic Ge within a crystalline GeTe matrix is confirmed at temperatures surpassing 325 °C. This is illustrated by the emergence of (111) and (220) peaks characteristic of cubic-Ge in Ge<sub>61</sub>Te<sub>39</sub> and Ge<sub>69</sub>Te<sub>31</sub>. Raoux et al. have demonstrated the sequential crystallization of GeTe and Ge, with the latter occurring at a higher temperature [66]. GeTe films exhibit diverse states due to control over deposition factors such as temperature, applied electric field on the substrate, seed layer structure, and deposition techniques (i.e., evaporation, sputtering, and epitaxial growth) [63]. GeTe films deposited below 130 °C typically exhibit an amorphous state. Deposited GeTe films adopt a polycrystalline state within the temperature range of 130 °C to 250 °C. If grown on a NaCl or mica seed layer at nearly 250 °C, GeTe forms a crystalline state with a rhombohedral structure. Above 250 °C, a crystalline GeTe film with a NaCl (or FCC) structure is observed [67–69].

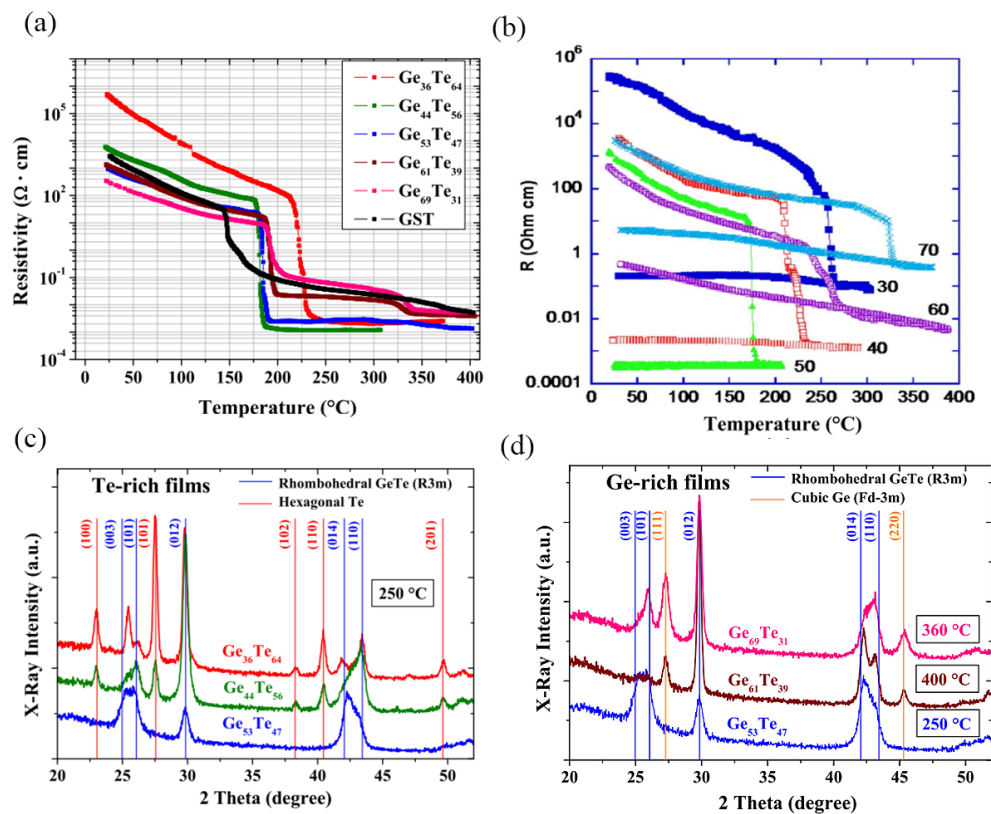


**Figure 4.** (a) Temperature-dependent resistivity measurements performed on 100 nm thin  $\text{Ge}_x\text{Te}_{100-x}$  films. The results reported are for a heating rate of 10  $^{\circ}\text{C}/\text{min}$  (adapted from [64]). (b) R–T curve for GeTe films of variable composition, with 30, 40, 50, 60, 70 at. % Ge (adapted from [65]). XRD patterns of (c) Te-rich samples and (d) Ge-rich samples (adapted from [64]). The smaller red dots represent Ge atoms and the larger yellow dots represent Te atoms.

By utilizing a 50:50 target for GeTe and adjusting the sputtering power and pressure, films can be produced with varying resistivity and crystallization temperature. GeTe films deposited at room temperature are initially amorphous. The crystalline GeTe film can be obtained by sputtering at elevated temperature or by annealing the as-deposited film. Sputtering power, deposition pressure, and Argon flow contribute to the resistance of GeTe, as shown in Figure 5a,b [70,71]. It is evident that higher sputtering power and lower pressure lead to lower crystalline resistance in most cases. In addition, the crystalline temperature changed as well with a different sputtering parameter. Figure 5c shows the scanning electronic image (SEM) of as-deposited and crystallized GeTe films [71]. The average grain size before crystallization is about 20 nm, but after crystallization the grain size increases by an order of magnitude (100–700 nm). The authors assumed that formation of voids is common in crystalline films, which may be due to densification within the film grains and the coalescence of micrometer- or nanometer-sized voids between grains. However, they have demonstrated that these voids do not have a deleterious effect on device performance when applied to PCSs with theses films. However, they have demonstrated that these voids do not adversely affect device performance when applied to PCSs with the film. Figure 5d illustrates the changes in the crystal state of GeTe during the annealing process [70]. As the temperature increases, the surface of GeTe will be the first to produce oxides of Ge and Te, followed by the formation of a thin oxide layer on the surface, and only below the oxide layer is a thin film of crystalline GeTe. However, if there is a passivation layer on the surface of GeTe, it is easy to avoid oxidation during annealing in the process of fabrication.

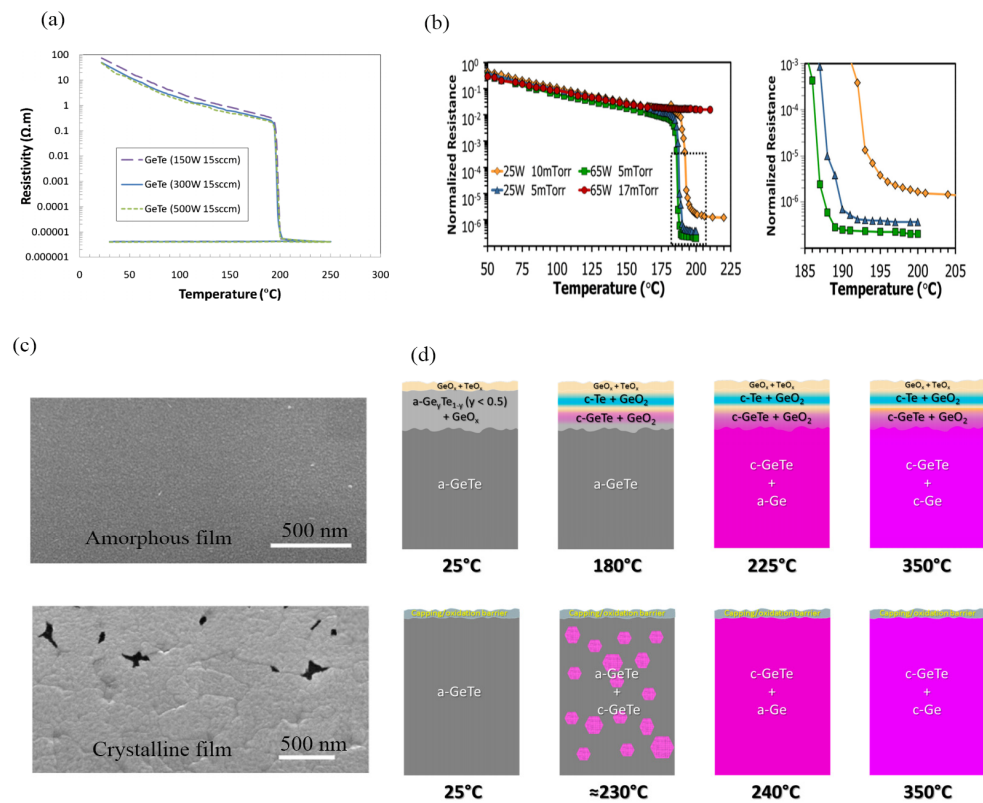


**Figure 5.** (a) Sheet resistance change in GeTe films annealed at elevated temperature with different sputtering power and Ar flow (adapted from [70]). (b) Normalized resistance in GeTe films at elevated temperature with different sputtering power and deposition pressure, and enlarged image of dashed area to show the transition temperature and final resistance value. (adapted from [71]). (c) SEM of amorphous and crystalline GeTe film (adapted from [71]). (d) Schematic representation of the surface-oxidized GeTe film during annealing with elevated temperatures and for the capped GeTe film (adapted from [72]).

### 3. GeTe-Based Phase-Change Switches (PCSs) for RF Application

In recent years, GeTe has been used as PCSs in RF applications, showing great potential due to its advantages, as seen in Table 1. According to the method of heating, phase-change switches are mainly divided into direct heating structures and indirect heating structures. The structure and performance of the two switches with different heating methods will be compared in next section.

#### 3.1. Comparison with Direct and Indirect Heating Structure Phase-Change Switches

This paper is the first to systematically analyze the stack structure of indirectly and directly heated phase-change RF switches, and analyze the roles of each functional layer other than the phase-change material, which will provide a reference for the optimization of device performance and future designs.

Figure 6a,b show the schematic diagram of the two types of stack structure for phase-change switches. In this review, GeTe is the constant phase-change material due to advantages for RF application. Both switches start with substrate and dielectric layer (bottom). In order to accommodate back-end-of-line (BEOL) processes for further integration, substrates such as HR-Si, Sapphire, SiC, GaAs, and GaN are optional.  $SiO_2$ ,  $SiN_x$ , and AlN film are also commonly used as dielectric layer for good insulation. A heater is used in both structures for raising the temperature of the phase-change layer. The phase-change transition results from the temperature rapidly rising and quenching or being kept continuous. The distinction between the two switches lies in the current flow mechanism: in a directly heated switch, the current flows through GeTe (the PCM) to heat itself, whereas in an indi-

rectly heated switch, the current passes through a microheater that generates heat, which is then conducted to the GeTe [18,23]. Materials used for the heater are metals such as TiW, TiN, NiCrSi, NiCr, W, Mo, etc. A stacking structure is used in an indirectly heated switch, as depicted in Figure 6b. The metal electrodes for the RF path are different combinations of Au or Cu and adhesion metals such as Ti, TiW, Cr, W, etc. The pros and cons of common materials used for each layer based on works reported so far will be analyzed.

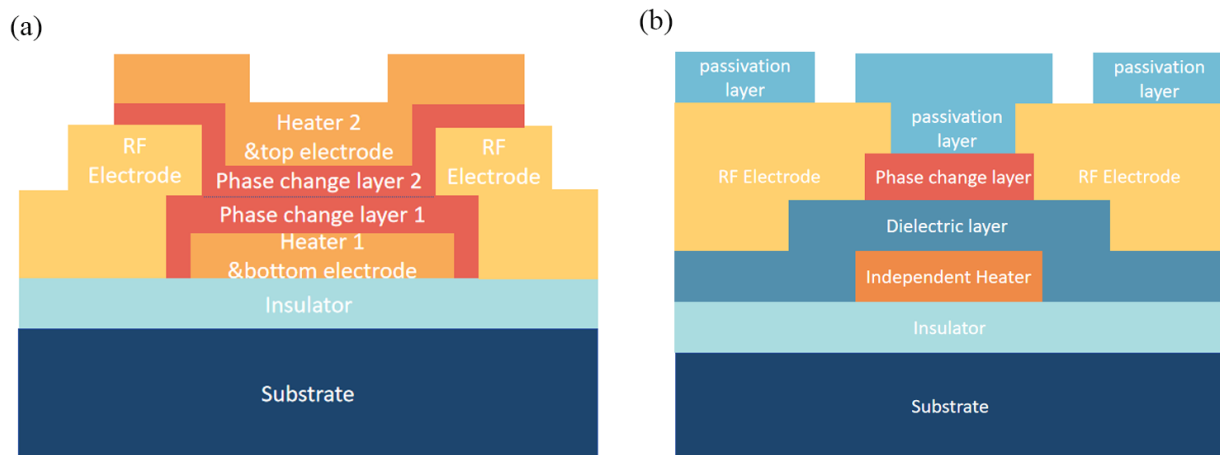


**Figure 6.** (a) Typical directly heated switch model illustrated (b) Typical indirectly heated switch model.

### 3.2. The Direct Heating Structure of Phase-Change Switches

Chua et al. first proposed a reconfigurable switch based on germanium tellurium in 2010 [70]. The GeTe reconfigurable phase-change switch has a low on-resistance of  $180 \Omega$  and a large dynamic range of  $7.2 \times 10^3$ . The GeTe switch has a diameter of  $1 \mu\text{m}$  and a thickness of  $100 \text{ nm}$ . The joule heat induced by the pulse current can convert the on-state to the off-state. The transition from off-state to on-state is achieved by Poole–Frenkel effect or the filament conductivity model [73–75]. The filament conductivity model used in the ovonic switching method explains the variation in  $R_{\text{ON}}$ , and a possible reason for partial re-amorphization and partial crystallization of the switch for the reduction in the dynamic range was proposed. The authors believe that this GeTe switch could be sufficient for many RF applications.

In 2013, Shim et al. [22] conducted a study on the RF characteristics of germanium telluride in phase-change switches. The research focused on critical RF performance of the switches, such as the third-order intercept point (IIP3) and the 1 dB compression point (P1dB), analyzing their behavior. The initial utilization of GeTe as a switch in the RF domain was realized, resulting in some observed RF performances. The extracted IIP3 in the crystalline state stood at  $37 \text{ dBm}$ , while in the amorphous state, it was approximately  $33 \text{ dBm}$ , with a frequency offset of  $50 \text{ kHz}$  at  $3.9 \text{ GHz}$ . Notably, the switch's linearity exhibited degradation at lower frequencies.

In 2014, Wang and Rais-Zadeh [23,24] introduced a directly heated four-terminal switch structure featuring dual RF ports (input and output) and a dedicated path for the heater. This switch exhibited an on-state insertion loss of less than  $0.5 \text{ dB}$  and off-state isolation exceeding  $18 \text{ dB}$  at frequencies up to  $20 \text{ GHz}$ , highlighting a cutoff frequency surpassing  $4 \text{ THz}$ . With a measured P1dB considerably greater than  $20 \text{ dBm}$  and an IIP3 exceeding  $30 \text{ dBm}$ , this architecture displayed impressive performance characteristics.

In 2019, Léon et al. [25,26] compared two configurations utilizing germanium telluride (GeTe) phase-change-material-based direct heating switches. Employing deep UV lithography stepper technology enabled the definition of consistent patterns with widths as narrow as  $250 \text{ nm}$ . For the first time, design guidelines were established linking the material geometry to the maximum allowable current through the switch before failure.

The study concluded that direct heating offers an efficient solution for GeTe amorphization, effectively preventing heater aging. Notably, in both configurations, a thick and short GeTe switch geometry was found to be advantageous. The shunt configuration achieved 31 dBm in the on-state and over 35 dBm in the off-state, while the series configuration achieved 27 dBm in the on-state and 32 dBm in the off-state. Moreover, the cutoff frequency for the shunt and series configurations reached 11 THz and 21 THz, respectively, at frequencies up to 40 GHz.

Figure 7a–c show three main models of direct heating structures: two-port and four-port sandwich structures and a four-port planar structure. Figure 7a is considered as a sandwich structure with a GeTe layer located in the middle of the heating electrodes. Figure 7b,c are schematic images of these sandwich structure of fabricated direct heating PCs. Figure 7c shows the planar connection structure of direct heating and the two configurations of shunt and series switches were applied in this configuration [19]. This structure has planar electrodes instead of bottom and top electrodes.

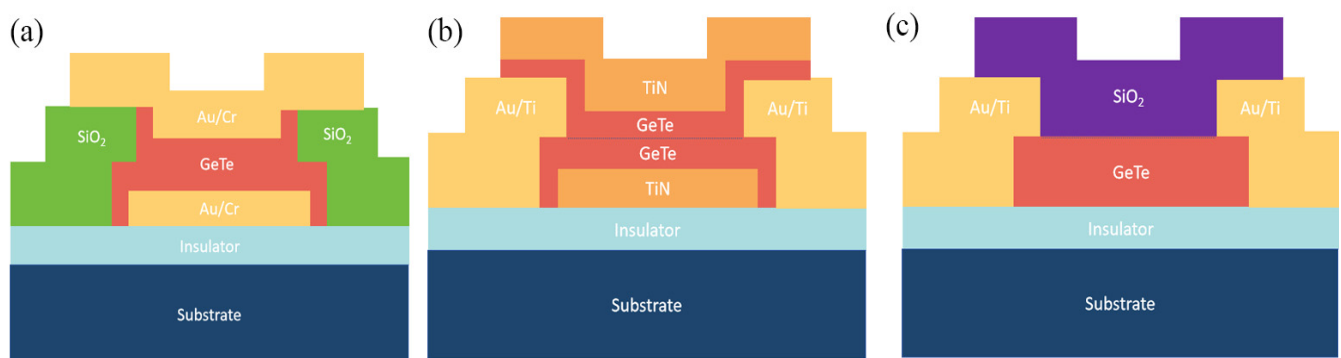


**Figure 7.** (a) Two-port directly heated model (adapted from [22]). (b) Four-port directly heated model [23]. (c) The image of the four-port planar structure GeTe direct heating switch (adapted from [26]).

### 3.3. The Indirect Heating Structure of Phase-Change Switches

Hinnawy et al. from Carnegie Mellon University introduced the concept of a four-terminal indirectly heated phase-change RF switch utilizing GeTe thin films in 2013 [76]. This groundbreaking concept exhibited remarkable RF capabilities and stability, subsequently gaining significant attention and adoption among subsequent researchers. Termed as the first generation, this four-terminal RF phase-change switch demonstrated a  $0.08 \Omega\text{-mm}$   $R_{ON}$  and a cut-off frequency ( $F_{CO}$ ) of 1.0 THz. Notably, it was the pioneering application of an electrically isolated heater to successfully activate both states of an inline phase-change switch. With excellent RF performance and stability, this indirectly heated structure has been heavily applied by subsequent scholars.

The process of the first generation is shown in Figure 8a, involving multiple steps: initially,  $\text{SiO}_2$  is formed on an HR-Si substrate, achieved through thermal growth or Plasma Enhanced Chemical Vapor Deposition (PECVD). Following this, NiCrSi thin film resistors are patterned using a stripping process. Subsequently, a dielectric barrier of  $\text{Si}_3\text{N}_4$  is established using PECVD, with the contact window in this layer etched via dry Reactive Ion Etch (RIE). GeTe film is deposited at room temperature via RF sputtering and patterned using the lift-off method, leading to its crystallization. Later, the Ti/Au contact and interconnect metallization layers are patterned by the lift-off technique. Finally, an additional PECVD  $\text{Si}_3\text{N}_4$  dielectric passivation is deposited, featuring dry-etched openings for electrical probing of the device. This design closely resembles a bottom-gated Field-Effect Transistor (FET), in which ohmic contacts are established with a channel material (the phase-change material or PCM) [77,78]. A thermally-isolated microheater is positioned beneath the chalcogenide channel, ensuring thermal coupling while maintaining dielectric isolation.

While the first generation (Gen1) process exhibited commendable RF performance, several critical issues persisted. Firstly, the NiCrSi heater, operating near its melting point (approximately 1200 K (approximately 1200 K), posed concerns regarding potential degradation of device performance and the likelihood of premature failure or damage [79]. Secondly, NiCrSi displays a negative resistance temperature coefficient, thereby diminishing the effective thermal width of the heater. Consequently, the electrical width of the melting region is reduced, subsequently curtailing the amorphization region and slowing down the switching speed. Lastly, amplifying the pulse power tends to decrease the lifespan of heater, directly impacting the device's reliability. To address these issues, the second generation (Gen2) of phase-change switches emerged, as depicted in Figure 8b. In this upgraded process, tungsten (W) serves as the microheater material due to its notably high melting point (approximately ~3700 K) and its linear, positive resistance temperature coefficient [80]. In contrast to the first generation, the performance of the second-generation phase-change switch has witnessed significant enhancements.

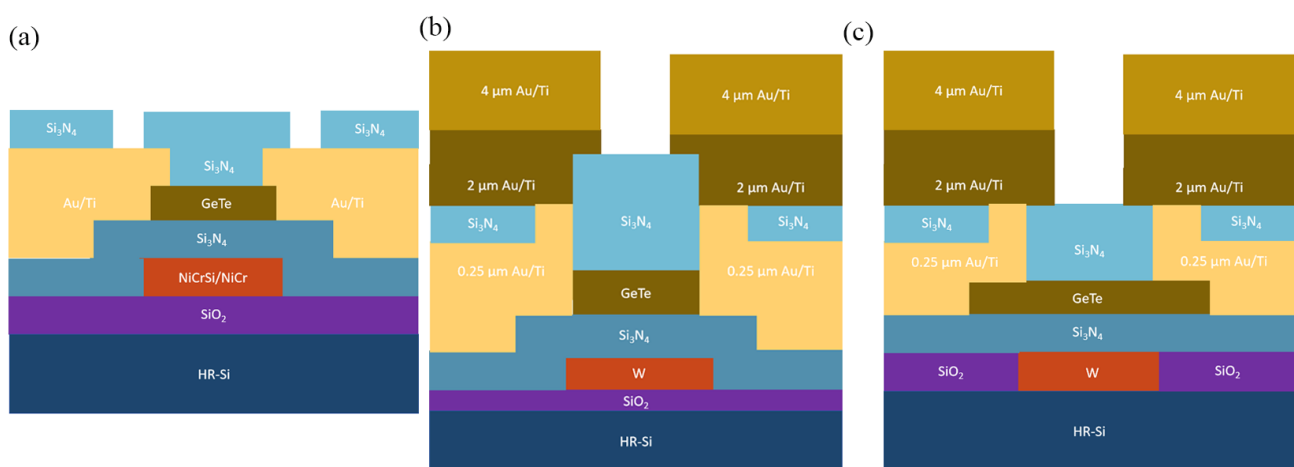


**Figure 8.** (a) The schematic cross-section of the Gen1 fabrication (adapted from [76]). (b) Schematic cross section of the Gen2 fabrication process (adapted from [77]). (c) Schematic cross section of the Gen3 fabrication process (adapted from [81]).

However, evident cracks along the microheater edges pose a significant challenge. This issue primarily arises due to stress induced by the deposition of GeTe films at room temperature followed by high-temperature annealing, leading to structural fissures. These cracks considerably impact the reliability of PCSs. To enhance RF performance while ensuring improved reliability, the third-generation process (Gen3) was developed, featuring a planar microheater architecture. Ti/TiN/W microheaters were crafted through an oxidation bath within an oxide trench using the damascene process. To maintain surface flatness, a chemical mechanical polishing technique (CMP) was employed on the top surface of the heater, as illustrated in Figure 8c. The thicker and flatter heater design of the third generation further enhances isolation between the control terminal and RF terminal. Moreover, it significantly reduces excitation pulse voltage requirements and lowers power consumption [81].

Although both types of switches have been investigated, indirectly heated PCSs are almost always used in current research on RF system applications, considering signal crosstalk and process integration issues. Table 2 lists some of the reported applications using indirectly heated PCSs.

**Table 2.** Excellent works on RF components based on GeTe film phase-change switches.

Components	Range (GHz)	RF Performance *: IL (Insertion Loss), ISO (Isolation), RL (Return Loss), PH (Power Handling), etc.
X-Band Reconfigurable bandpass filters [82]	7.45–8.07	IL: 2.6–3.2 dB IIP <sub>3</sub> **: 30 dBm Tuning speed: <6 μs
6-bit latching switched capacitor bank [83]	2–7	Capacitance tuning range: 0.14 pF to 8 pF Capacitance ratio: 58:1 Tuning speed: 1.4 μs
4-bit Latching Variable Attenuator [84]	24–32	Maximum attenuation: 37 dB Minimum attenuation: 4.7 dB RL: >20 dB
Switched K-Band Tunable Reflective Load [85]	DC–60	The resonance: <18 GHz or > 26.5 GHz Phase shift: 30° at 18 GHz and up to 45° at 26.5 GHz
3-bit switched True-Time-Delay phase Wideband shifters [86]	26–34	Phase shifter at 30 GHz: 170° (ps-a), 173° (ps-b) IL <sub>max</sub> : 4.9 dB (ps-a), 4.7 dB (ps-b) RL <sub>min</sub> : 16.5 dB (ps-a), 14 dB (ps-b)
Integrated Wideband Digital Switched Attenuator [87]	26–34	Attenuation range: 24.1 dB IL: 3.9 dB, RL <sub>min</sub> : 13 dB PH: 35.5 dBm, IIP <sub>3</sub> : 4.1 dBm
Reflection-Type Phase Shifter With 8-Bit Switched Phase Tuning [88]	26–30	Phase shifter at 30 GHz: 280° IL <sub>max</sub> : 6 dB RL <sub>min</sub> : 14.2 dB;
Monolithic Band Reject Circuit [89]	1–8	Four states of this circuit: reject f <sub>1</sub> at 2.6 GHz; reject f <sub>2</sub> at 5.8 GHz; reject f <sub>1</sub> and f <sub>2</sub> at the same time; no rejection IL < 2.2 dB RL > 17 dB
Switch matrix [90]	DC–60	IL < 3 dB, RL > 14 dB, ISO > 20 dB
R-type and C-type Switch [91]	DC–30	C-type: IL < 0.75 dB, RL > 18 dB R-type: IL < 1.1 dB (state I/II), <1.5 dB (state III), RL > 18 dB, ISO > 25 dB
T-type switch [92]	DC–67	IL < 0.6 dB, RL > 20 dB, ISO > 20 dB
DPDT (Double-Pole, Double-Throw) Switch [93]	DC–20	IL < 2 dB (0–5 GHz), IL < 4 dB (@20 GHz) ISO > 17.5 dB (0–20 GHz)
SPNT (Single-Pole, N-Throw) Switches [94]	DC–40	SP2T: IL < 0.5 dB (0–20 GHz), IL < 0.7 dB (0–40 GHz) ISO > 26 dB (0–40 GHz) SP4T: IL < 0.6 dB (0–20 GHz), IL < 1 dB (0–40 GHz) ISO > 25 dB (0–40 GHz) SP9T: IL < 0.5 dB (0–20 GHz), IL < 1.5 dB (0–40 GHz) ISO > 28 dB (0–40 GHz)

\* IL: Insertion Loss; ISO: isolation; RL: Return Loss; PH: Power Handling. \*\* IIP<sub>3</sub>: third-order intercept point.

### 3.3.1. Substrate and Insulator Layer

For substrates suitable for phase-change switching, good heat dissipation, good high-frequency transmission characteristics, and good matching to the film are required. Typically for semiconductor substrates, an additional insulating layer is required to minimize charge crosstalk at high frequencies. In the current preparation of switching devices, the substrates that have been used are HR-Si, Sapphire, SiC, Alumina, etc. [19,28,32,79,95]. and insulators often used are SiO<sub>2</sub>, SiN<sub>x</sub>, AlN [23,28,75,96–100]. AlN can also be a heat spreader to reduce the consumption of PCSs [101]. Table 3 lists the commonly used combinations of substrate and insulator. In RF switches, the relative permittivity of substrate significantly influences overall RF performance. Concurrently, the thermal conductivity of the substrate plays a crucial role in determining the required drive voltage for the switch. Carriers

within the semiconductor exhibit increased mobility, accelerating the response speed to the current, and consequently elevating conductivity levels. Therefore, an insulating layer is frequently employed to mitigate electrical crosstalk originating from the substrate at elevated frequencies.

**Table 3.** Common substrates and insulating materials used in RF switches.

Substrate (Sub)	Thermal Conductivity (W/m·K)	Relative Permittivity of Sub	Insulator	Refs.
HR-Si			SiO <sub>2</sub>	[23,95,100]
HR-Si	150	11.9	SiN <sub>x</sub>	[99]
HR-Si			AlN	[19]
SiC	120–490	10	SiO <sub>2</sub>	[79]
Alumina	18–35	11.5	SiO <sub>2</sub>	[28]
Sapphire	25–40	9.8	N/A	[32]
GaAs	46	12.5	N/A	[97]
GaN	9	150	N/A	[98]

### 3.3.2. Heater Layer

In PCS applications, the phase-change material undergoes a transformation between two distinct states: the amorphous state characterized by high resistance (OFF) and the crystalline state characterized by low resistance (ON). To transition the phase-change material (GeTe) into the “OFF” amorphous state requires heating it above its melting temperature (730 °C) and subsequently rapidly cooling it (typically achieved with a thermal RC time constant less than 100 ns) to drop it below the crystallization temperature. The process of transitioning the same material into the “ON” state is comparatively less demanding, as heating it to a temperature below the melting point combined with a duration longer than 30 ns is often adequate to crystallize the material. Thus, taking the PC material into the amorphous state requires greater electrical power to achieve higher temperatures as well as switch design that permits cooling in a time constant shorter than 100 ns to prevent crystallization. This process places the greater constraints on the electrical drive as well as the switch architecture. A heater physically separated from the switch can be used to turn the switch on or off by producing a desired temperature. The heater must be capable of being driven, with sufficient power at high speed so that one can reach temperatures above 730 °C and cool sufficiently fast. The transient temperature of the heater is an issue of great concern to scholars, and finite-element modeler (FEM) simulation softwares like Comsol 5.5 and Ansys workbench 2019 are advantageous tools for these investigations. As can be seen from Figure 9, a microheater is required to generate heat by the joule effect and pass the heat to the PCM to implement the phase-change process.

Experiments have demonstrated that TiW, W, TiN, NiCrSi, NiCr, and Mo are all candidates for microheaters in PCSs, as shown Figure 10a. To achieve the melting point of GeTe, varying widths of heaters with different metal materials were simulated using Comsol 5.5 [26]. From the simulation result, a wider heater width generates a lower max temperature at constant thickness, and Mo generates more heat than W and Cr. Figure 10b illustrate the impact of varying heater widths on both MPA (minimum power to amorphize) and MPC (minimum power to crystallize), alongside the influence on the off-state capacitance ( $C_{OFF}$ ) [32]. The MPA escalates by 0.5 W for every micron increase in heater width, while the MPC rises by 0.1 W per micrometer. This increase in power can be attributed to the amplified heating volume, subsequently leading to an upsurge in thermal capacitance and thermal time constant. Consequently, to liquefy PC material within the same 100 ns voltage pulse, an elevation in the power supplied to the heater becomes necessary, corresponding the result of Figure 10a. Moreover,  $C_{OFF}$  experiences an increase of 4.3 fF per micrometer of increase of heater width. Therefore, a wider heater width increases the power consumption of PCSs. Figure 10c delineates the impact of the

switch heater size on insertion loss (IL) and isolation (Iso). These measurement results conform to the trends observed in simulation outcomes from another report, as depicted in Figure 10d [26]. Therefore, a preliminary conclusion is drawn that a smaller heater width results in lower IL, and higher Iso and return loss (RL).

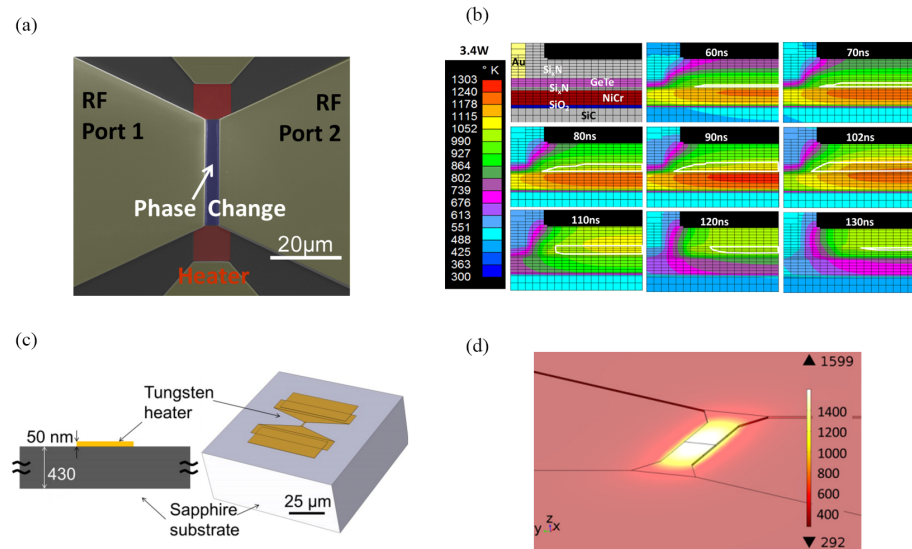


**Figure 9.** (a) Colored SEM of a GeTe phase-change RF switch (adapted from [79]). (b) Simulated progression of the heat pulse from the heater into the GeTe layer, with the melt zone delineated by the white borders by Ansys (adapted from [79]). (c) Cross-sectional view of the device and Comsol perspective view of the device (adapted from [102]). (d) Perspective view of the simulated temperature map of the heater (adapted from [102]).

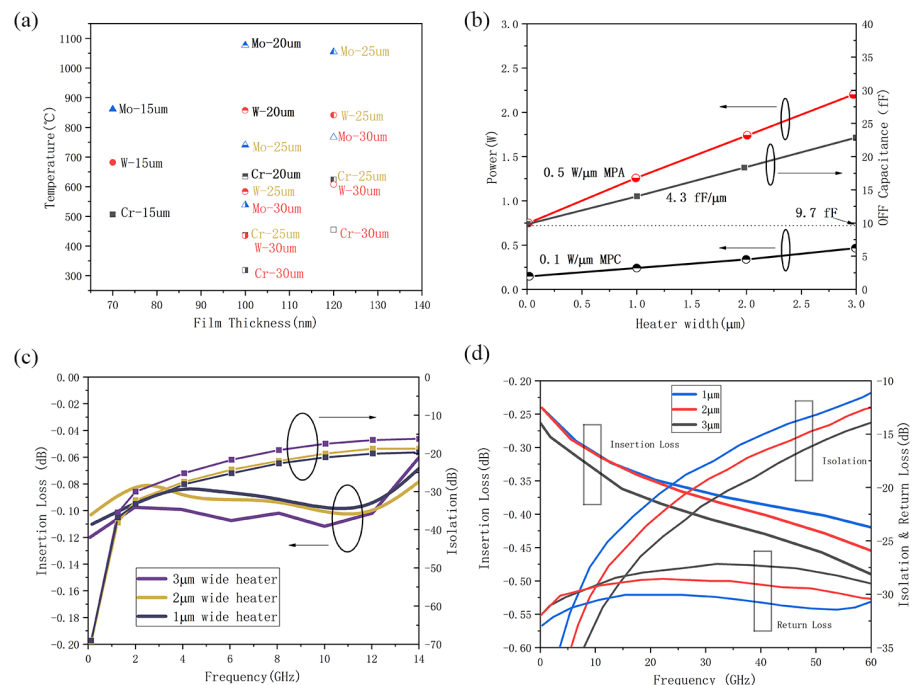


**Figure 10.** (a) Simulated temperatures for 15, 20, and 25 nm-wide chromium, tungsten, and molybdenum microheaters with thicknesses of 70, 100, and 150 nm (data from [32]). (b) MPA, MPC, and Extracted  $C_{OFF}$  for 20 μm switches with heater widths of 1, 2, and 3 μm (data from [103]). (c) Measured insertion loss and isolation with heater widths of 1, 2, and 3 μm from 45 MHz to 14 GHz (data from [103]). (d) Insertion loss, isolation and return loss EM simulation of the PCM switch with heater widths of 1, 2, and 3 μm (Data from [32]).

To address the necessity for efficient thermal conduction in phase-change RF switches, the resistive material constituting the heating layer assumes a pivotal role in the thermally induced phase-change process. Table 4 presents a compilation of candidate materials suitable for the heating layer of phase-change switches. It is noteworthy that, given compatibility with the process, the choice of material for PCSs relies on possessing the suitable heat capacity and resistivity.

**Table 4.** Materials used as microheater in GeTe-based PCSs.

Material	Thermal Conductivity (W/m·K)	Melting Point (°C)	Resistivity ( $\Omega \cdot m$ )	Type	Refs.
Mo	142	2610	$5.2 \times 10^{-8}$	indirect	[93]
AlCu	104	670	$2.5 \times 10^{-8}$	direct	[21,22]
W	174	3390	$5.0 \times 10^{-8}$	indirect	[26,32,84,91]
NiCr	12.2	1350	$1.1 \times 10^{-6}$	indirect	[28]
NiCrSi	-	-	-	indirect	[18,67,68,93]
TiN	19.2	2950	$2.0 \times 10^{-7}$	indirect	[27]
TiN	19.2	2950	$2.0 \times 10^{-7}$	direct	[19,20]

### 3.3.3. Dielectric Layer

The dielectric layer in a PCS functions to isolate the heating path from the RF path while facilitating efficient heat transfer to the GeTe film. It necessitates excellent insulation properties alongside high thermal conductivity. Effective insulation prevents interference or crosstalk between the DC activating pulse and RF transmission signal. Simultaneously, high thermal conductivity enables rapid heat conduction from the heating layer to the phase-change material, facilitating the phase change within the nanosecond-level pulse duration. Commonly employed dielectric materials in PCSs encompass  $\text{SiO}_2$ ,  $\text{SiN}_x$ , AlN, and others. Table 5 shows the dielectric material used in PCSs. High resistivity and melting point are essential properties for dielectric layer materials to ensure effective insulation and thermal stability. Furthermore, research indicates that AlN with its high thermal conductivity, plays a beneficial role in enhancing switch speed and reducing DC drive power consumption [94].

**Table 5.** Dielectric materials used in PCSs.

Dielectric Material	Thermal Conductivity (W/m·K)	Melting Temperature (°C)	Resistivity ( $\Omega \cdot m$ )	Refs.
$\text{SiO}_2$	1.4	1700	$10^{12} \sim 10^{14}$	[17–23,31]
$\text{SiN}_x$	3	1900	$10^9 \sim 10^{12}$	[90]
AlN	140	2500	$10^{10} \sim 10^{14}$	[23,102,104]

Figure 11a,b depict that the implementation of AlN film as the dielectric layer exhibits lower MPA and heater temperature compared to  $\text{SiN}_x$  for a fixed  $F_{co}$  (cutoff frequency), which represents the FOM (figure of merit) and is defined as  $F_{co} = 1/(2\pi \times R_{ON}C_{OFF})$ , where  $R_{ON}$  is the on-state resistance and  $C_{OFF}$  is the off-state capacitance [94]. Reduced MPA holds particular significance in numerous RF systems where generating high DC voltages proves either inaccessible or economically burdensome. To achieve a higher  $F_{co}$ , elevating the heater temperature beyond half of the melting point of W (3665 K) is necessary, which can potentially degrade the dielectric layer. It can be seen that at the same  $F_{co}$ , the switch with AlN has a smaller MPA than a switch using  $\text{SiN}_x$ , which can reduce the power consumption of the device. In addition, AlN is more heat-proof compared to  $\text{SiN}_x$ , contributing to enhanced reliability for PCSs. Figure 11c shows that both switches exhibit on-state resistance of  $2 \Omega$  up to 15 GHz. Altering the AlN barrier thickness from 105 nm to

170 nm results in a reduction of the off-state capacitance from 15 fF to 10 fF [95]. Figure 11d delves into the impact of dielectric layer thickness on RF performance via simulation. It becomes apparent that a thicker dielectric layer leads to reduced IL, increased Iso, and diminished RL. This relationship implies a trade-off between IL and Iso [32].

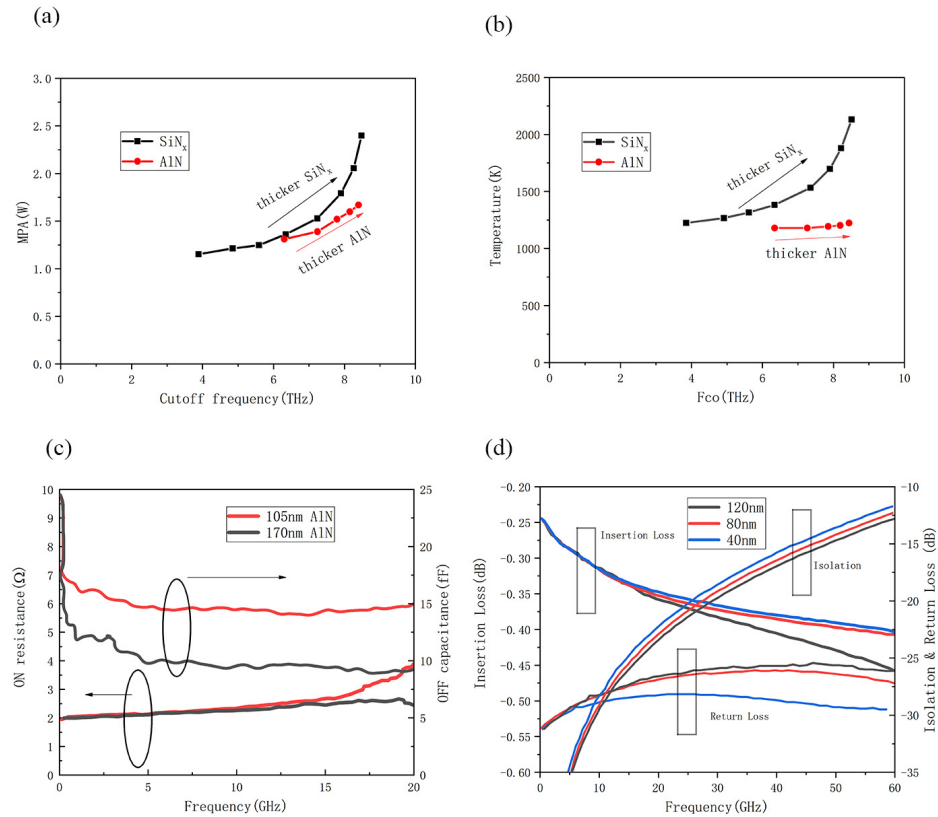


**Figure 11.** (a) Simulated MPA and (b) simulated maximum heater temperature as a function of F<sub>CO</sub> for a 1.06 μm-wide heater, where SiN<sub>x</sub> thickness ranged from 20 nm to 155 nm while AlN was between 70 nm and 200 nm (data from [104]). (c) R<sub>ON</sub> and C<sub>OFF</sub> of 105 nm and 170 nm AlN film from DC-20 GHz (data from [104]). (d) Insertion loss, isolation and return loss EM simulation of the PCM switch with a variation in barrier thickness (Data from [32]).

### 3.3.4. RF Electrode

The RF electrode serves to establish a connection with the phase-change material (PCM), contributing to the resistance variation of GeTe and facilitating the transmission of RF signals. The gap length ( $L_{PCM}$ ) between the two RF electrodes significantly impacts the resistance of the  $R_{ON}$ . According to the relationship  $R = \rho L_{PCM} / S$  (where  $\rho$  represents resistivity),  $R_{ON}$  is directly proportional to the  $L_{PCM}$ . Consequently, a smaller  $L_{PCM}$  results in a reduced  $R_{ON}$ . However, concurrently considering  $C_{OFF}$ , determined by the equation  $C = \epsilon S / L_{PCM}$  (where  $\epsilon$  represents relative permittivity),  $C_{OFF}$  is inversely proportional to the  $L_{PCM}$ . Therefore, in the design of  $L_{PCM}$ , considerations for both  $R_{ON}$  and  $C_{OFF}$  are essential. Achieving smaller  $R_{ON}$  requires a smaller gap, whereas the optimization of  $C_{OFF}$  necessitates a larger gap length. Balancing these factors becomes crucial in the design phase of  $L_{PCM}$  in RF electrode configuration.

Figure 12a,b show the MPA and MPC, respectively, for switches with  $L_{PCM}$  from 400 nm to 800 nm. As the  $L_{PCM}$  decreases, the MPA increases. This is because Au contacts are closer together and absorb more heat from the PC material. To compensate for the increased heat dissipation, more power is needed to raise the temperature of the PC material above its melting temperature [103]. Figure 12c,d show the  $R_{ON}$  and  $C_{OFF}$ , respectively, extracted from 45 MHz to 20 GHz [32,103]. As expected, the  $R_{ON}$  decreases as the  $L_{PCM}$  decreases. As the  $L_{PCM}$  decreases from 800 nm to 400 nm, the  $R_{ON}$  decreases from 3 to 1.4 Ω. However, as

$R_{ON}$  decreases,  $C_{OFF}$  also increases from 11.7 to 15.4 fF. Figure 12d exhibits the simulation of RF performance for different gap lengths, and it can be seen that the smaller gap results in smaller insertion loss, but also smaller isolation and smaller return loss. There is a trade-off between  $R_{ON}$  and  $C_{OFF}$  as well as insertion loss and isolation.

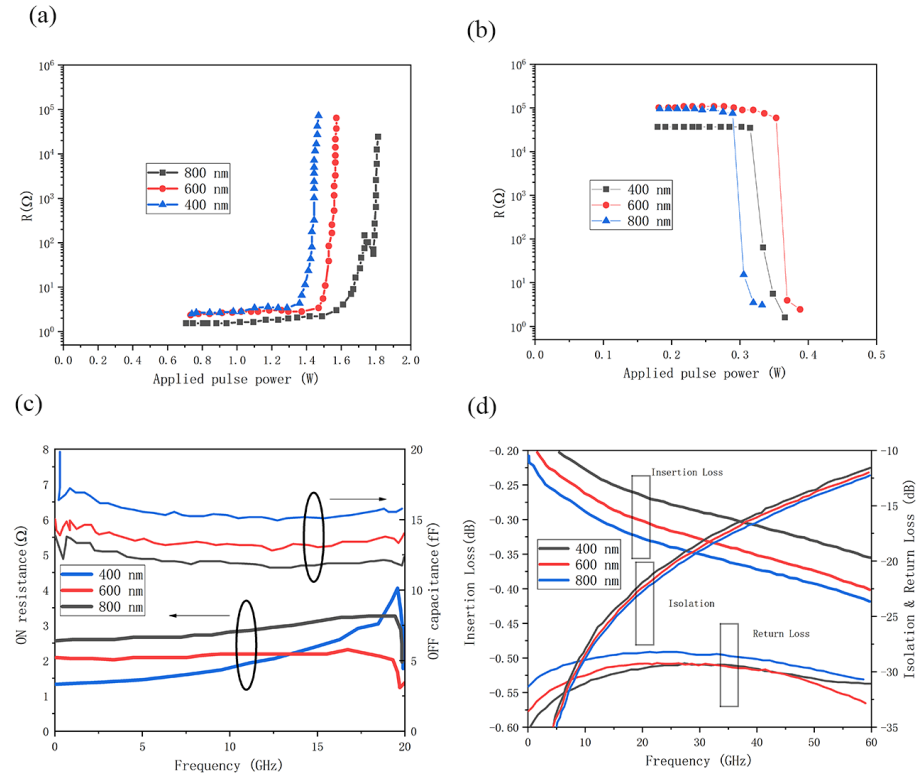


**Figure 12.** (a) MPA and (b) MPC results for 20  $\mu\text{m}$ -wide switches with RF gaps ranging from 400 to 800 nm in length (data from [103]). (c) Extracted  $R_{ON}$  and  $C_{OFF}$  of switches with varying  $L_{PCM}$  from 45 MHz to 20 GHz (data from [103]). (d) Insertion loss, isolation, and return loss EM simulation of the PCM switch with a variation in channel length (data from [32]).

Device architectures often require GeTe to be in contact with metal electrodes. Hence, the performance of these devices is notably susceptible to the influence of metal/GeTe interfaces. This scenario holds particular significance in GeTe-based RF switches, where studies indicate that contact resistance ( $R_c$ ) contributes significantly, accounting for 20–50% of the on-state resistance of the switch [105]. Table 6 demonstrates the test data on the contact resistance as well as the specific contact resistance of commonly used electrodes to GeTe. Considering the aforementioned data, achieving an ohmic contact between the electrode layer and GeTe becomes a critical inclusion in the optimization process of the switch design.

**Table 6.** Contact resistance and specific contact resistivity of GeTe and metal [105,106].

Contact Metal	Contact Resistance $R_c$ ( $\Omega \cdot \text{mm}$ )	Specific Contact Resistivity $\rho_c$ ( $\Omega \cdot \text{cm}^2$ )	Sheet Resistance $R_{sh}$ ( $\Omega/\text{sq}$ )
Pd/Ti/Pt/Au	$0.0036 \pm 0.002$	$(3.7 \pm 0.2) \times 10^{-9}$	36
Mo/Ti/Pt/Au	$0.0035 \pm 0.001$	$(3.6 \pm 0.7) \times 10^{-9}$	38
Ni/Ti/Pt/Au	$0.016 \pm 0.003$	$(6.4 \pm 2.2) \times 10^{-8}$	40
Sn/Fe/Au	$0.0037 \pm 0.001$	$(5.2 \pm 0.6) \times 10^{-9}$	43
Ti/Pt/Au	$0.034 \pm 0.0028$	$(3.13 \pm 0.6) \times 10^{-7}$	38
TiW/Al	$0.0054 \pm \dots$	$(1.43 \pm \dots) \times 10^{-8}$	...
Cr/Pt/Au	$0.0055 \pm 0.002$	$(9.6 \pm 0.8) \times 10^{-9}$	36
W/Al	$0.0054 \pm \dots$	$(1.4 \pm \dots) \times 10^{-8}$	...

#### 4. Conclusions

The utilization of chalcogenides in communication, storage, thermoelectricity, and various other domains is increasingly pervasive. Compared to representative RF switches, PCS boasts a host of advantages, including superior RF performance, high linearity, enhanced integration capabilities, non-volatile characteristics, and rapid switching speeds. Focused on phase-change RF switches, Ge<sub>50</sub>Te<sub>50</sub> is selected as the core phase-change material through the screening of different stoichiometric composition. Based on the current researches, possible structures of GeTe in crystalline and amorphous states are detailed below.

The crystalline structure of GeTe film includes a distorted rock salt (R-GeTe) structure and a face-centered cubic (C-GeTe) structure. GeTe films deposited below 130 °C typically exhibit an amorphous state. Deposited GeTe films adopt a polycrystalline state within the temperature range of 130 °C to 250 °C. If grown on a NaCl or mica seed layer at nearly 250 °C, GeTe forms a single-crystalline with a rhombohedral structure. Above 250 °C, GeTe film presents a single-crystalline with an FCC structure, while the amorphous structure of GeTe film is surrounded by the combination of tetrahedral and defect octahedral configurations. Amorphous Ge<sub>2</sub>Sb<sub>2</sub>Te<sub>5</sub> is characterized by even-folded ring structures, whereas amorphous GeTe has both even- and odd-numbered rings. The possible patterns of tetrahedral structure are as follows: 6.25% GeTe<sub>4</sub>, 25% GeTe<sub>3</sub>Ge, 37.5% GeTe<sub>2</sub>Ge, 2.25% GeTeGe<sub>3</sub>, and 6.25% GeGe<sub>4</sub>.

This paper offers a comprehensive comparative analysis of two prevalent structures of phase-change RF switches: direct heating structures and indirect heating structures. Although both types of switches have been investigated, indirectly heated switches are dominant in current research on RF system applications, considering signal crosstalk and process integration issues. Based on existing literatures, this paper also summarized material selection for each layer and the dimensions or thicknesses of switches within these layers. The resulting conclusions of RFPCSs are as follows:

- (1) The relative permittivity and of substrate significantly influences overall RF performance. Concurrently, the thermal conductivity of the substrate plays a crucial role in determining the required drive voltage for the switch.
- (2) The heater must be capable of being driven, with sufficient power at high speed so that one can reach temperatures above 730 °C and cool sufficiently fast. A wider heater width would increase the power consumption of the PCS. A preliminary conclusion is drawn that a smaller heater width results in lower insertion loss (IL), and higher isolation (Iso) and return loss (RL).
- (3) The thicker dielectric layer could decrease C<sub>OFF</sub> but increase power consumption for a higher MPA. AlN could lower power consumption for PCSs compared to a device using SiN<sub>x</sub>. It becomes apparent that a thicker dielectric layer leads to reduced IL, increased Iso, and diminished RL. This relationship implies a trade-off between IL and Iso.
- (4) There is a trade-off between R<sub>ON</sub> and C<sub>OFF</sub> and insertion loss and isolation for the gap width of the RF transmission electrodes. Obviously, as the gap decreases, the insertion loss decreases, but so does the isolation and return loss. In addition, the effect of contact resistance due to the interaction of the electrodes with the GeTe must be considered.

#### 5. Outlook

Over the past decade, RFPCS technology has rapidly developed for application in reconfigurable RF front-end systems. The excellent features of easy integration and low power consumption allow PCSs to make a big impact up to millimeter-wave frequencies. There has been a succession of excellent works on RF components based on phase-change switching application. Although the current GeTe-based PCSs have many excellent features, there are still a lot of areas that can be improved, such as switching speed, power handling capability, endurance, etc. In this review, the influence and role of each layer on

switching performance has been analyzed, and it is believed that this review can provide a corresponding reference for enhancing performance in future communications.

After extensive research efforts, significant strides have been achieved in advancing the development and utilization of GeTe RFPCSs. Progress has been notable across structural design, materials utilization, and process optimization, transitioning from the initial direct heating configuration to the more refined indirect heating architecture. This latter approach has undergone iterative changes from its initial introduction to its current state as a third-generation model. With the development of integration process and micron/nano scale fabrication technology, it will certainly be more perfect. The future process direction of RF-PCSs is mainly along the monolithic or heterogeneous integration. The GeTe phase-change RF switches exhibit three pivotal characteristics: high cutoff frequency, non-volatility, and compatibility with back-end processes. These distinctive features render these switches highly advantageous tools for augmenting flexibility across a spectrum of technological domains, including millimeter-wave networks, sub-6G wireless systems, reconfigurable architectures, and passive circuits. Moreover, these switches serve as integral components in the construction of reconfigurable devices, employed as discrete packaging elements. They are anticipated to supplant commonly utilized PIN diodes in specific scenarios, representing a rare occurrence in their application as discrete packaging components within reconfigurable device architecture. In military applications, leveraging GeTe phase-change RF switches facilitates the development of customized field-programmable gate arrays (FPGAs) designed specifically for constructing adaptable devices. These advancements hold the potential for cost savings within military communication, electronic warfare, and intelligence systems, as they capitalize on the capabilities offered by field-programmable gate array (FPGA) RF front-end components grounded on GeTe phase-change RF switches.

**Author Contributions:** All authors participated in the literature research of the review. The categorization of the literature was done by S.Q. and J.W. The first draft of the manuscript was written by S.Q. and all authors commented on previous versions of the manuscript. All authors have read and agreed to the published version of the manuscript.

**Funding:** This research received no external funding.

**Data Availability Statement:** No new data were created or analyzed in this study. Data sharing is not applicable to this article.

**Conflicts of Interest:** The authors declare no conflicts of interest.

## References

1. Daneshmand, M. Multi-Port RF MEMS Switches and Switch Matrices. Ph.D. Thesis, University of Waterloo, Waterloo, ON, Canada, 2006.
2. Rebeiz, G.M. *RF MEMS: Theory, Design, and Technology*; John Wiley & Sons: Hoboken, NJ, USA, 2004.
3. Chauffleur, X.; Rabbia, L.; Pons, P.; Grenier, K.; Plana, R.; Dantas, L.; Flourens, F.; Kuchenbecker, J.; Dubuc, D.; Boukabache, A. Effect of membrane shape on mechanical behavior of RF switches. *Sens. Actuators A Phys.* **2004**, *112*, 148. [[CrossRef](#)]
4. Gong, Y.; Teng, J.W.; Cressler, J.D. A Compact, High-Power, 60 GHz SPDT Switch Using Shunt-Series SiGe PIN Diodes. In Proceedings of the IEEE Radio Frequency Integrated Circuits Symposium, Boston, MA, USA, 2–4 June 2019; pp. 15–18.
5. Kumar, J.; Basu, B.; Talukdar, F.A. Modeling of a PIN Diode RF Switch for Reconfigurable Antenna Application. *Sci. Iran.* **2019**, *26*, 1714–1723.
6. Wu, Z.; Lu, W.; Bao, X.; Meng, F.; Yang, Z.; Sun, Q.; Zhao, F.; Wang, Y. Study on cut-off characteristics of sub-nanosecond silicon carbide PiN switch. *Int. J. Mod. Phys. B* **2021**, *35*, 150107. [[CrossRef](#)]
7. Yang, X.; Lin, J.; Chen, G.; Kong, F. Frequency reconfigurable antenna for wireless communications using GaAs FET switch. *IEEE Antennas Wirel. Propag. Lett.* **2015**, *14*, 807–810. [[CrossRef](#)]
8. Mizutani, H.; Takayama, Y. DC-110-GHz MMIC traveling-wave switch. *IEEE Trans. Microw. Theory Tech.* **2000**, *48*, 840–845. [[CrossRef](#)]
9. Souchon, F.; Saint-Patrice, D.; Pornin, J.L.; Bouchu, D.; Baret, C.; Reig, B. Thin film packaged redundancy RF MEMS switches for space applications. In Proceedings of the 19th International Conference on Solid-State Sensors, Actuators and Microsystems, Kaohsiung, Taiwan, 18–22 June 2017; pp. 175–178.
10. Angira, M.; Rangra, K. Design and investigation of a low insertion loss, broadband, enhanced self and hold down power RF-MEMS switch. *Microsyst. Technol.* **2015**, *21*, 1173–1178. [[CrossRef](#)]

11. Zhu, Y.Q.; Han, L.; Wang, L.F.; Tang, J.Y.; Huang, Q.A. A Novel Three-State RF MEMS Switch for Ultrabroadband (DC–40 GHz) Applications. *IEEE Electron Device Lett.* **2013**, *34*, 1062–1064. [[CrossRef](#)]
12. Stegmaier, M.; Ríos, C.; Bhaskaran, H.; Wright, C.D.; Pernice, W.H.P. Nonvolatile All-Optical  $1 \times 2$  Switch for Chipscale Photonic Networks. *Adv. Opt. Mater.* **2017**, *5*, 1600346. [[CrossRef](#)]
13. Tanaka, D.; Shoji, Y.; Kuwahara, M.; Wang, X.; Kintaka, K.; Kawashima, H.; Toyosaki, T.; Ikuma, Y.; Tsuda, H. Ultra-Small, Self-Holding, Optical Gate Switch Using Ge<sub>2</sub>Sb<sub>2</sub>Te<sub>5</sub> with a Multi-Mode Si Waveguide. *Opt. Express* **2012**, *20*, 10283. [[CrossRef](#)]
14. Zhang, Y.; Chou, J.B.; Li, J.; Li, H.; Du, Q.; Yadav, A.; Zhou, S.; Shalaginov, M.Y.; Fang, Z.; Zhong, H.; et al. Broadband Transparent Optical Phase Change Materials for High-Performance Nonvolatile Photonics. *Nat. Commun.* **2019**, *10*, 4279. [[CrossRef](#)]
15. Mikulics, M.; Hardtdegen, H.H. Fully Photon Operated Transmistor / All-Optical Switch Based on a Layered Ge<sub>1</sub>Sb<sub>2</sub>Te<sub>4</sub> Phase Change Medium. *FlatChem* **2020**, *23*, 100186. [[CrossRef](#)]
16. Zheng, J.; Zhu, S.; Xu, P.; Dunham, S.; Majumdar, A. Modeling Electrical Switching of Nonvolatile Phase-Change Integrated Nanophotonic Structures with Graphene Heaters. *ACS Appl. Mater. Interfaces* **2020**, *12*, 21827–21836. [[CrossRef](#)] [[PubMed](#)]
17. Ghosh, R.R.; Dhawan, A. Integrated Non-Volatile Plasmonic Switches Based on Phase-Change-Materials and Their Application to Plasmonic Logic Circuits. *Sci. Rep.* **2021**, *11*, 18811. [[CrossRef](#)]
18. Shim, Y.; Hummel, G.; Rais-Zadeh, M. RF switches using phase change materials. In Proceedings of the IEEE 26th International Conference on Micro Electro Mechanical Systems (MEMS), Taipei, Taiwan, 20–24 January 2013; pp. 237–240.
19. Wang, M.; Rais-Zadeh, M. Directly heated four-terminal phase change switches. In Proceedings of the IEEE MTT-S International Microwave Symposium-IMS, Tampa, FL, USA, 1–6 June 2014; pp. 1–4.
20. Wang, M.; Shim, Y.; Rais-Zadeh, M. A low-loss directly heated two-port RF phase change switch. *IEEE Electron Device Lett.* **2014**, *35*, 491–493. [[CrossRef](#)]
21. Leon, A.; Reig, B.; Perret, E.; Podevin, F.; Saint-Patrice, D.; Puyal, V.; Lugo-Alvarez, J.; Ferrari, P. RF Power-Handling Performance for Direct Actuation of Germanium Telluride Switches. *IEEE Trans. Microw. Theory Tech.* **2020**, *68*, 60–73. [[CrossRef](#)]
22. Leon, A.; Navarro, G.; Puyal, V.; Reig, B.; Podevin, F.; Ferrari, P.; Perret, E. In-depth characterization of the structural phase change of Germanium Telluride for RF switches. In Proceedings of the IEEE MTT-S International Microwave Workshop Series on Advanced Materials and Processes for RF and THz Applications (IMWS-AMP), Pavia, Italy, 20–22 September 2017.
23. El-Hinnawy, N.; Borodulin, P.; Jones, E.B.; Wagner, B.P.; Young, R.M. 12.5 THz F<sub>co</sub> GeTe inline phase-change switch technology for reconfigurable RF and switching applications. In Proceedings of the IEEE Compound Semiconductor Integrated Circuit Symposium (CSICS), La Jolla, CA, USA, 19–22 October 2014; pp. 1–3.
24. Moon, J.S.; Seo, H.C.; Le, D.; Fung, H.; Yang, B. 10.6 THz figure-of-merit phase-change RF switches with embedded micro-heater. In Proceedings of the IEEE Topical Meeting on Silicon Monolithic Integrated Circuits in RF Systems, San Diego, CA, USA, 26–28 January 2015; pp. 73–75.
25. Moon, J.S.; Seo, H.C.; Son, K.A.; Lee, K.; Tai, H. 5 THz figure-of-merit reliable phase-change RF switches for millimeter-wave applications. In Proceedings of the IEEE/MTT-S International Microwave Symposium-IMS, Philadelphia, PA, USA, 10–15 June 2018; pp. 836–838.
26. Fu, S.S.; Gao, L.; Peng, Y.; Qu, S.; Wang, J.; Chen, H.; Liu, N.; Zhang, J. Novel four-port RF phase change switches based on GeTe thin film. *J. Micromechanics Micro Eng.* **2023**, *33*, 095004. [[CrossRef](#)]
27. Ghalem, A.; Hariri, A.; Guines, C.; Passerieux, D.; Huitema, L.; Blondy, P.; Crunteanu, A. Arrays of GeTe electrically activated RF switches. In Proceedings of the IEEE MTT-S International Microwave Workshop Series on Advanced Materials and Processes for RF and THz Applications (IMWS-AMP), Pavia, Italy, 20–22 September 2017; pp. 1–3.
28. Singh, T.; Mansour, R.R. A Miniaturized Monolithic PCM Based Scalable Four-Port RF Switch Unit-Cell. In Proceedings of the 49th European Microwave Conference (EuMC), Paris, France, 1–3 October 2019; pp. 180–183.
29. Huber, E.; Marinero, E.E. Laser-induced crystallization of amorphous GeTe: A time-resolved study. *Phys. Rev. B* **1987**, *36*, 1595–1604. [[CrossRef](#)]
30. Ghalem, A.; Guines, C.; Passerieux, D.; Orlianges, J.C.; Huitema, L.; Crunteanu, A. Reversible, fast optical switching of phase change materials for active control of high-frequency functions. In Proceedings of the IEEE/MTT-S International Microwave Symposium-IMS, Philadelphia, PA, USA, 10–15 June 2018; pp. 839–842.
31. El-Hinnawy, N.; Borodulin, P.; Wagner, B.P.; King, M.R.; Jones, E.B.; Howell, R.S.; Lee, M.J.; Young, R.M. Low-loss latching microwave switch using thermally pulsed non-volatile chalcogenide phase change materials. *Appl. Phys. Lett.* **2014**, *105*, 013501. [[CrossRef](#)]
32. Singh, T.; Mansour, R.R. Characterization, Optimization, and Fabrication of Phase Change Material Germanium Telluride Based Miniaturized DC–67 GHz RF Switches. *IEEE Trans. Microw. Theory Tech.* **2019**, *67*, 3237–3250. [[CrossRef](#)]
33. Kohara, S.; Kato, K.; Kimura, S.; Tanaka, H.; Usuki, T.; Suzuya, K.; Tanaka, H.; Moritomo, Y.; Matsunaga, T.; Yamada, N.; et al. Structural basis for the fast phase change of Ge<sub>2</sub>Sb<sub>2</sub>Te<sub>5</sub>. Ring statistics analogy between the crystal and amorphous states. *Appl. Phys. Lett.* **2006**, *89*, 201910. [[CrossRef](#)]
34. Ren, K.; Duan, X.; Xiong, Q.; Li, Y.; Song, Z. Constructing reliable PCM and OTS devices with an inter-facial carbon layer. *J. Mater. Sci. Mater. Electron.* **2019**, *30*, 20037–20042. [[CrossRef](#)]
35. Yu, H.; Du, Y. Increasing Endurance and security of phase-change memory with multi-way wear-leveling. *IEEE Trans. Comput.* **2019**, *63*, 1157–1168.

36. Lama, G.; Bourgeois, G.; Bernard, M.; Castellani, N.; Sandrini, J.; Nolot, E.; Garrione, J.; Cyrille, M.C.; Navarro, G.; Nowak, E. Reliability analysis in GeTe and GeSbTe based phase-change memory 4 kb arrays targeting storage class memory applications. *Microelectron. Reliab.* **2020**, *114*, 113823. [[CrossRef](#)]
37. Park, S.; Kim, T.; Hwang, S.; Park, D.; Ahn, M.; Cho, M.H. In situ thermal behavior of resistance drift in GeTe and Ge<sub>2</sub>Sb<sub>2</sub>Te<sub>5</sub> nanowires via raman thermometry. *J. Mater. Chem. C* **2020**, *8*, 11032–11041. [[CrossRef](#)]
38. Kunkel, T.; Vorobyov, Y.; Smayev, M.; Lazarenko, P.; Veretennikov, V.; Sigaev, V.; Kozyukhin, S. Experimental observation of two-stage crystallization of Ge<sub>2</sub>Sb<sub>2</sub>Te<sub>5</sub> amorphous thin films under the influence of a pulsed laser. *J. Alloys Compd.* **2021**, *851*, 156924. [[CrossRef](#)]
39. Moon, J.S.; Sun, J.; Seo, H.C.; Son, K.A.; Lee, K.; Zehnder, D.; Tai, H.; Le, D. Phase-change RF switches with robust switching cycle endurance. In Proceedings of the IEEE Radio and Wireless Symposium, Anaheim, CA, USA, 15–18 January 2018.
40. Yalon, E.; Datye, I.M.; Moon, J.S.; Son, K.A.; Lee, K.; Pop, E. Energy-efficient indirectly heated phase change RF switch. *IEEE Electron Device Lett.* **2019**, *40*, 455–458. [[CrossRef](#)]
41. Mennai, A.; Bessaudou, A.; Cosset, F.; Guines, C.; Blondy, P.; Aurelian, C. Bistable RF switches using Ge<sub>2</sub>Sb<sub>2</sub>Te<sub>5</sub> phase change material. In Proceedings of the IEEE 2015 European Microwave Conference, Paris, France, 7–10 September 2015; pp. 945–947.
42. Field, M.; Hillman, C.; Stupar, P.; Hacker, J.; Griffith, Z.K.; Lee, J. Vanadium dioxide phase change switches. In Proceedings of the International Society for Optics and Photonic, Baltimore, MD, USA, 20–24 April 2015.
43. Kovitz, J.M.; Allen, K.W. Recent Developments toward reconfigurable mmwave apertures and components using vanadium dioxide RF switches. In Proceedings of the IEEE 19th Wireless and Microwave Technology Conference (WAMICON), Sand Key, FL, USA, 9–10 April 2018; pp. 1–4.
44. Pan, K.; Wang, W.; Shin, E.; Freeman, K.; Subramanyam, G. Vanadium oxide thin-film variable resistor-based RF switches. *IEEE Trans. Electron Devices* **2015**, *62*, 2959–2965.
45. Chattopadhyay, T.; Pannetier, J.; Schnering, H.G.V. Neutron diffraction study of the structural phase transition in SnS and SnSe. *J. Phys. Chem. Solids* **1986**, *47*, 879–885. [[CrossRef](#)]
46. Deringer, V.L.; Dronskowski, R.; Wuttig, M. Microscopic Complexity in Phase-Change Materials and its Role for Applications. *Adv. Funct. Mater.* **2015**, *25*, 6343–6359. [[CrossRef](#)]
47. Sosman, R.B. *The Phases of Silica*; Rutgers University Press: New Brunswick, NJ, USA, 1965.
48. Zheng, Z.; Su, X.; Deng, R.; Stoumpos, C.; Xie, H.; Liu, W.; Yan, Y.; Hap, S.; Uher, C.; Wolverton, C.; et al. Rhombohedral to Cubic Conversion of GeTe via MnTe Alloying Leads to Ultralow Thermal Conductivity, Electronic Band Convergence, and High Thermoelectric Performance. *J. Am. Chem. Soc.* **2018**, *140*, 2673–2686. [[CrossRef](#)]
49. Ali, A.; Ansari, S.M.; Ehab, B.; Mohammad, B.; Anjum, D.H.; Aldosari, H.M. Effect of vacuum annealing on structural and electrical properties of germanium telluride thin films. *Mater. Res. Bull.* **2022**, *146*, 111575. [[CrossRef](#)]
50. Yu, N.N.; Tong, H.; Miao, X.S. Structure and phonon behavior of crystalline GeTe ultrathin film. *Appl. Phys. Lett.* **2014**, *105*, 121902. [[CrossRef](#)]
51. Liu, W.D.; Wang, D.Z.; Liu, Q.F.; Zhou, W.; Shao, Z.P.; Chen, Z.G. High-Performance GeTe-Based Thermoelectrics: From Materials to Devices. *Adv. Energy Mater.* **2020**, *10*, 2000367. [[CrossRef](#)]
52. Hong, M.; Zou, J.; Chen, Z.G. Thermoelectric GeTe with Diverse Degrees of Freedom Having Secured Superhigh Performance. *Adv. Mater.* **2019**, *31*, 1807071. [[CrossRef](#)] [[PubMed](#)]
53. Xing, G.Z.; Sun, J.F.; Li, Y.W.; Fan, X.F.; Zheng, W.T.; Singh, D.J. Thermoelectric properties of p-type cubic and rhombohedral GeTe. *J. Appl. Phys.* **2018**, *123*, 195105. [[CrossRef](#)]
54. Kolobov, A.V.; Fons, P.; Frenkel, A.I.; Ankudinov, A.L.; Tominaga, J.; Uruga, T. Understanding the phase-change mechanism of rewritable optical media. *Nat. Mater.* **2004**, *3*, 703–708. [[CrossRef](#)]
55. Welnic, W.; Pamungkas, A.; Detemple, R.; Steimer, C.; Blügel, S.; Wuttig, M. Unravelling the interplay of local structure and physical properties in phase-change materials. *Nat. Mater.* **2006**, *5*, 56–62. [[CrossRef](#)]
56. Kolobov, A.V.; Fons, P.; Tominaga, J. Understanding Phase-Change Memory Alloys from a Chemical Perspective. *Sci. Rep.* **2015**, *5*, 13698. [[CrossRef](#)]
57. Andrikopoulos, K.S.; Yannopoulos, S.N.; Voyiatzis, G.A.; Kolobov, A.V.; Ribes, M.; Tominaga, J. Raman scattering study of the a-GeTe structure and possible mechanism for the amorphous-to-crystal transition. *J. Phys.-Condens. Matter* **2006**, *18*, 965–979. [[CrossRef](#)]
58. Sun, C.; Tay, B.K.; Zeng, X.; Li, S.; Chen, T.; Zhou, J.; Bai, H.; Jiang, E. Bond-order-bond-length-bond-strength (bond-OLS) correlation mechanism for the shape-and-size dependence of a nanosolid. *J. Phys.-Condens. Matter* **2002**, *14*, 7781–7795. [[CrossRef](#)]
59. Andrikopoulos, K.S.; Yannopoulos, S.N.; Kolobov, A.V.; Fons, P.; Tominaga, J. Raman scattering study of GeTe and Ge<sub>2</sub>Sb<sub>2</sub>Te<sub>5</sub> phase-change materials. *J. Phys. Chem. Solids* **2017**, *68*, 1074–1078. [[CrossRef](#)]
60. Deringer, V.L.; Zhang, W.; Lumeij, M.; Maintz, S.; Wuttig, M.; Mazzarello, R.; Dronskowski, R. Bonding Nature of Local Structural Motifs in Amorphous GeTe. *Angew. Chem. Int. Ed.* **2014**, *53*, 10817–10820. [[CrossRef](#)]
61. Mazzarello, R.; Caravati, S.; Angioletti-Uberti, S.; Bernasconi, M.; Parrinello, M. Signature of Tetrahedral Ge in the Raman Spectrum of Amorphous Phase-Change Materials. *Phys. Rev. Lett.* **2011**, *107*, 085503. [[CrossRef](#)]
62. Wdowik, U.D.; Parlinski, K.; Rols, S.; Chatterji, T. Soft-phonon mediated structural phase transition in GeTe. *Phys. Rev. B* **2014**, *89*, 224306. [[CrossRef](#)]

63. Sengottaiyan, R.; Saxena, N.; Shukla, K.D.; Manivannan, A. Temperature dependent structural evolution and crystallization properties of thin Ge<sub>15</sub>Te<sub>85</sub> film revealed by in situ resistance, X-ray diffraction and scanning electron microscopic studies. *J. Phys. D Appl. Phys.* **2020**, *53*, 205108. [[CrossRef](#)]
64. Navarro, G.; Sousa, V.; Persico, A.; Pashkov, N.; Toffoli, A.; Bastien, J.C.; Perniola, L.; Maitrejean, S.; Roule, A.; Zuliani, P.; et al. Material engineering of Ge<sub>x</sub>Te<sub>100-x</sub> compounds to improve phase-change memory performances. *Solid State Electron.* **2013**, *89*, 93–100. [[CrossRef](#)]
65. Raoux, S.; Muñoz, B.; Cheng, H.Y.; Jordan-Sweet, J.L. Phase transitions in Ge–Te phase change materials studied by time-resolved x-ray diffraction. *Appl. Phys. Lett.* **2009**, *95*, 143118. [[CrossRef](#)]
66. Raoux, S.; Cheng, H.Y.; Caldwell, M.A.; Wong, H.S.P. Crystallization times of GeTe phase change materials as a function of composition. *Appl. Phys. Lett.* **2009**, *95*, 071910. [[CrossRef](#)]
67. Hyot, B.; Biquard, X.; Poupinet, L. Local structures of morphous and crystalline GeTe and GeSbTe. In Proceedings of the EPCOS, Lugano, Switzerland, 10–11 March 2003.
68. Chopra, K.L.; Bahl, S.K. Amorphous versus Crystalline GeTe Films. I. Growth and Structural Behavior. *Phys. Rev. B* **2006**, *73*, 045210. [[CrossRef](#)]
69. Wang, M. Phase Change Material Based Ohmic Switches for Reconfigurable RF Applications. Ph.D. Thesis, University of Michigan, Ann Arbor, MI, USA, 2017.
70. Chua, E.K.; Shi, L.P.; Zhao, R.; Lim, K.G.; Chong, T.C.; Schlesinger, T.E.; Bain, J.A. Low resistance, high dynamic range reconfigurable phase change switch for radio frequency applications. *Appl. Phys. Lett.* **2010**, *97*, 418–419. [[CrossRef](#)]
71. King, M.R.; Wagner, B.P.; Jones, E.B.; El-Hinnawy, N.; Borodulin, P.; McLaughlin, S.R.; Mason, J.S.; Howell, R.S.; Lee, M.J.; Young, R.M. Development of cap-free sputtered GeTe films for inline phase change switch based RF circuits. *J. Vac. Sci. Technol. B* **2014**, *32*, 041204. [[CrossRef](#)]
72. Kolb, A.N.D.; Bernier, N.; Robin, E.; Benayad, A.; Rouvière, J.-L.; Sabbione, C.; Hippert, F.; Noé, P. Understanding the Crystallization Behavior of Surface-Oxidized GeTe Thin Films for Phase-Change Memory Application. *ACS Appl. Electron. Mater.* **2019**, *1*, 701–710. [[CrossRef](#)]
73. Shim, Y.; Rais-Zadeh, M. Non-Linearity analysis of RF ohmic switches based on phase change materials. *IEEE Electron Device Lett.* **2014**, *35*, 405–407. [[CrossRef](#)]
74. Ielmini, D.; Zhang, Y. Analytical model for subthreshold conduction and threshold switching in chalcogenide-based memory devices. *J. Appl. Phys.* **2007**, *102*, 662–667. [[CrossRef](#)]
75. Kostylev, S.A. Threshold and Filament Current Densities in Chalcogenide-Based Switches and Phase-Change-Memory Devices. *IEEE Trans. Electron Devices* **2009**, *30*, 814–816. [[CrossRef](#)]
76. El-Hinnawy, N.; Borodulin, P.; Wagner, B.P.; King, M.R.; Mason, J.S.; Jones, E.B.; Veliadis, V.; Howell, R.S.; Young, R.M.; Lee, M.J. A 7.3 THz cut-off frequency, inline, chalcogenide phase-change RF switch using an independent resistive heater for thermal actuation. In Proceedings of the IEEE Compound Semiconductor Integrated Circuit Symposium (CSICS), Monterey, CA, USA, 13–16 October 2013; pp. 1–4.
77. Suresh, R.; Borodulin, P.; El-Hinnawy, N.; Kuss, F.C.; Young, R.M.; Howell, R.S.; Lee, M. Low-loss non-volatile phase-change RF switching technology for system reconfigurability and reliability. In Proceedings of the Architecture/Open Business Model Net-Centric Systems and Defense Transformation, Baltimore, MD, USA, 5–9 May 2014; Volume 9096.
78. El-Hinnawy, N.; Borodulin, P.; Wagner, B.; King, M.R.; Mason, J.S.; Jones, E.B.; McLaughlin, S.; Veliadis, V.; Snook, M.; Sherwin, M.E.; et al. A Four-Terminal, Inline, Chalcogenide Phase-Change RF Switch Using an Independent Resistive Heater for Thermal Actuation. *IEEE Electron Device Lett.* **2013**, *34*, 1313–1315. [[CrossRef](#)]
79. Young, R.M.; El-Hinnawy, N.; Borodulin, P.; Wagner, B.P.; King, M.R.; Jones, E.B.; Howell, R.S.; Lee, M.J. Thermal analysis of an indirectly heat pulsed non-volatile phase change material microwave switch. *J. Appl. Phys.* **2014**, *116*, 054504. [[CrossRef](#)]
80. Desai, P.D.; Chu, T.K.; James, H.M.; Ho, C.Y. Electrical Resistivity of Selected Elements. *J. Phys. Chem. Ref. Data* **1984**, *13*, 1069–1096. [[CrossRef](#)]
81. El-Hinnawy, N.; Borodulin, P.; King, M.R.; Padilla, C.R.; Ezis, A.; Nichols, D.T.; Paramesh, J.; Bain, J.A.; Young, R.M. Origin and Optimization of RF Power Handling Limitations in Inline Phase-Change Switches. *IEEE Trans. Electron Devices* **2017**, *64*, 3934–3942. [[CrossRef](#)]
82. Wang, M.; Lin, F.; Rais-Zadeh, M. An X-band reconfigurable bandpass filter using phase change RF switches. In Proceedings of the IEEE 16th Topical Meeting on Silicon Monolithic Integrated Circuits in RF Systems (SiRF), Austin, TX, USA, 24–27 January 2016; pp. 38–41.
83. Singh, T.; Mansour, R.R. Reconfigurable PCM GeTe-Based Latching 6-Bit Digital Switched Capacitor Bank. In Proceedings of the European Microwave Integrated Circuits Conference, Milan, Italy, 26–27 September 2022.
84. Singh, T.; Mansour, R.R. Miniaturized Reconfigurable 28 GHz PCM-Based 4-Bit Latching Variable Attenuator for 5G mmWave Applications. In Proceedings of the IEEE MTT-S International Microwave Symposium, Los Angeles, CA, USA, 4–6 August 2020.
85. Singh, T.; Mansour, R.R. Chalcogenide GeTe-Based Non-Volatile Switched K-Band Tunable Reflective Load for Reconfigurable RF Circuits. In Proceedings of the IEEE/MTT-S International Microwave Symposium, Denver, CO, USA, 19–24 June 2022; pp. 967–970.
86. Singh, T.; Mansour, R.R. Loss compensated pcm GeTe-based latching wideband 3-bit switched true-time-delay phase shifters for mmwave phased arrays. *IEEE Trans. Microw. Theory Tech.* **2020**, *68*, 3745–3755. [[CrossRef](#)]

87. Singh, T.; Mansour, R.R. Scalable mmwave non-volatile phase change GeTe-based compact monolithically integrated wideband digital switched attenuator. *IEEE Trans. Electron Devices* **2021**, *68*, 2306–2312. [[CrossRef](#)]
88. Singh, T.; Mansour, R.R. Compact 26–30 GHz Reflection-Type Phase Shifter With 8-Bit Switched Phase Tuning Utilizing Chalcogenide Phase-Change Switches. *IEEE Trans. Microw. Theory Tech.* **2023**, *71*, 193–202. [[CrossRef](#)]
89. Singh, T.; Mansour, R.R. Reconfigurable and Scalable Monolithic Band Reject Circuit Utilizing Phase-Change Switch Matrices. In Proceedings of the 16th European Microwave Integrated Circuits Conference (EuMIC), London, UK, 3–4 April 2021; pp. 34–37.
90. Singh, T.; Mansour, R.R. Miniaturized DC–60 GHz RF PCM GeTe-based monolithically integrated redundancy switch matrix using T-type switching unit cells. *IEEE Trans. Microw. Theory Tech.* **2019**, *67*, 5181–5190. [[CrossRef](#)]
91. Singh, T.; Mansour, R.R. Non-volatile multiport DC–30 GHz monolithically integrated phase-change transfer switches. *IEEE Electron Device Lett.* **2021**, *42*, 867–870. [[CrossRef](#)]
92. Singh, T.; Mansour, R.R. Monolithic PCM Based Miniaturized T-type RF Switch for Millimeter Wave Redundancy Switch Matrix Applications. In Proceedings of the IEEE MTT-S International Microwave Symposium (IMS), Boston, MA, USA, 2–7 June 2019; pp. 658–660.
93. Hariri, A.; Crunteanu, A.; Guines, C.; Hallepee, C.; Passerieux, D.; Blondy, P. Double-port double-throw (DPDT) switch matrix based on phase change material (PCM). In Proceedings of the 48th European Microwave Conference (EuMC), Madrid, Spain, 23–27 September 2018; pp. 479–482.
94. Slovin, G.; El-Hinnawy, N.; Masse, C.; Rose, J.; Howard, D. Multi-Throw SPNT Circuits Using Phase-Change Material RF Switches for 5G and Millimeter Wave Applications. In Proceedings of the IEEE MTT-S International Microwave Symposium (IMS), Atlanta, GA, USA, 7–25 June 2021; pp. 428–430.
95. King, M.R.; El-Hinnawy, N.; Borodulin, P.; Ezis, A.; Luu, V.; Salmon, M.; Gu, J.; Nichols, D.T.; Dickey, E.; Maria, J.-P.; et al. Connecting post-pulsing electrical and microstructural features in GeTe-based inline phase change switches. *J. Appl. Phys.* **2018**, *124*, 195103. [[CrossRef](#)]
96. Wang, M.; Lin, F.; Rais-Zadehm, M. Performance measurements and non-linearity modeling of GeTe phase change RF switches with direct and indirect heating schemes. In Proceedings of the IEEE MTT-S International Microwave Symposium, Phoenix, AZ, USA, 17–22 May 2015.
97. Suemune, I.; Uesugi, K.; Kumano, H. Study of light emitters with capability of multi-wavelength emissions in visible and infrared wavelength ranges on GaAs substrates. *Photonics Based Wavel. Integr. Manip.* **2005**, *2*, 71–92.
98. Majumdar, S.; Biswas, D. Evaluating substrate's effect on RF switch performance via Verilog-a GaN HEMT model. *Microelectron J.* **2017**, *62*, 43–48. [[CrossRef](#)]
99. Gao, L.; Liu, M.; Qu, S.; Liu, J.; Fu, S.; Ding, Y.; Chen, H.; Zhang, J. Nano-Scanning Calorimetry Applied to Phase Change Processes in GeTe Thin Films. *IEEE Trans. Electron Devices* **2023**, *70*, 4128–4132. [[CrossRef](#)]
100. King, M.R.; El-Hinnawy, N.; Salmon, M.; Gu, J.; Wagner, B.P.; Jones, E.B.; Borodulin, P.; Howell, R.S.; Nichols, D.T.; Young, R.M. Morphological analysis of GeTe in inline phase change switches. *J. Appl. Phys.* **2015**, *118*, 094501. [[CrossRef](#)]
101. El-Hinnawy, N.; Borodulin, P.; King, M.R.; Furrow, C.; Padilla, C.R.; Ezis, A.; Nichols, D.T.; Paramesh, J.; Bain, J.A.; Young, R.M. Experimental Demonstration of AlN Heat Spreaders for the Monolithic Integration of Inline Phase-Change Switches. *IEEE Electron Device Lett.* **2018**, *39*, 610–613. [[CrossRef](#)]
102. Xu, M.; Slovin, G.; Paramesh, J.; Schlesinger, T.E.; Bain, J.A. Thermometry of a high temperature high speed micro heater. *Rev. Sci. Instrum.* **2016**, *87*, 164–167. [[CrossRef](#)]
103. Slovin, G.; Xu, M.; Singh, R.; Schlesinger, T.E.; Paramesh, J.; Bain, J.A. Design Criteria in Sizing Phase-Change RF Switches. *IEEE Trans. Microw. Theory Tech.* **2017**, *65*, 4531–4540. [[CrossRef](#)]
104. Slovin, G.; Xu, M.; Paramesh, J.; Schlesinger, T.E.; Bain, J.A. AlN Barriers for Capacitance Reduction in Phase-Change RF Switches. *IEEE Electron Device Lett.* **2016**, *37*, 568–571. [[CrossRef](#)]
105. Chua, E.K.; Zhao, R.; Shi, L.P.; Chong, T.C.; Schlesinger, T.E.; Bain, J.A. Effect of metals and annealing on specific contact resistivity of GeTe/metal contacts. *Appl. Phys. Lett.* **2012**, *101*, 012107. [[CrossRef](#)]
106. Cooley, K.A.; Aldosari, H.M.; Yang, K.; Mohny, S.E. Review of electrical contacts to phase change materials and an unexpected trend between metal work function and contact resistance to germanium telluride. *J. Vac. Sci. Technol. A* **2020**, *38*, 050805. [[CrossRef](#)]

**Disclaimer/Publisher's Note:** The statements, opinions and data contained in all publications are solely those of the individual author(s) and contributor(s) and not of MDPI and/or the editor(s). MDPI and/or the editor(s) disclaim responsibility for any injury to people or property resulting from any ideas, methods, instructions or products referred to in the content.